THESIS

DETECTION AND RELOCATION OF EARTHQUAKES IN THE SPARSELY INSTRUMENTED MACKENZIE MOUNTAINS REGION, YUKON AND NORTHWEST TERRITORIES, CANADA

Submitted by

David C. Heath

Department of Geosciences

In partial fulfillment of the requirements

For the Degree of Master of Science

Colorado State University

Fort Collins, Colorado

Spring 2020

Master's Committee:

Advisor: Derek L. Schutt

Richard C. Aster
David J. Wald
Margaret Cheney

ABSTRACT

DETECTION AND RELOCATION OF EARTHQUAKES IN THE SPARSELY INSTRUMENTED MACKENZIE MOUNTAINS REGION, YUKON AND NORTHWEST TERRITORIES, CANADA

The Mackenzie Mountains are an actively uplifting and seismogenic arcuate thrust belt lying within the Northwest Territories and Yukon, Canada. Seismic activity in the region is poorly constrained due to a historically sparse seismograph distribution. In this study, new data are analyzed from the 40-station, ~875 km-long Mackenzie Mountains temporary network (Baker et al., 2020) crossing the Cordillera-Craton region adjacent to and within the Mackenzie Mountains, in conjunction with Transportable Array and other sparsely distributed arrays in the region. Data from approximately August 2016 – August 2018 are processed and compared to the sparse-network earthquake catalog records maintained by the USGS and Natural Resources Canada. Using algorithms developed by Kushnir et al. (1990), Rawles and Thurber (2015), and Roecker et al. (2006), signals are identified and subsequently associated across the network to note potential events, estimate phase onsets, and resolve hypocenter locations. This study improves the regional earthquake catalog by detecting smaller-magnitude earthquakes and lowering the regional magnitude of completeness from M_c = 2.5 to 1.9. Within the Mackenzie Mountains and immediately surrounding areas we find 524 new events and additionally recommend an updated location for 185 previously cataloged events. Our *b*-value computation for the updated catalog (0.916 ± 0.08) likely indicates a relatively high level of regional differential stress. We identify the spatial distribution of earthquakes in the Mackenzie Mountains as diffuse, and offer far-field stress transfer as a mechanism for producing widespread reverse faulting observed in the region. Further, we associate regional seismicity with tectonic activity in the context of known faults and orogenic provinces such as the Richardson Mountains.

ACKNOWLEDGEMENTS

I would like to thank my advisor, Dr. Derek Schutt for his invaluable guidance during the completion of this project. I would additionally like to thank my Committee Members for their comments and well-regarded opinions about improvements to this work. Many thanks also go to my fellow graduate students, whose advice, musings, and good company I will always value. Additional thanks to my family and other friends who have been wholly supportive of me during my time at Colorado State University. I would also like to acknowledge the First Nations peoples from the many Tribes whose land was used for this seismic experimentation. I am deeply grateful for the opportunity to learn about their history and culture alongside my research. Lastly, thank you to the National Science Foundation for their support of this project with EarthScope grant EAR-1460533.

TABLE OF CONTENTS

ABSTRACT ii
ACKNOWLEDGEMENTS iii
LIST OF TABLES vi
LIST OF FIGURES vii

Chapter 1 Introduction and Background 1
1.1 Geologic Setting 1
1.2 Seismic Background 4
1.3 MMEP Experiment 6
1.3.1 Project Motivation 6
1.3.2 Instrumentation 7
1.3.3 Deployment 8
1.3.4 Servicing 9
1.3.5 Demobilization 10
1.3.6 Downtime 10
1.4 Earthquake Detection Methodology 11
1.4.1 General Theory 12
1.4.2 Experimental Workflow 13
1.4.3 Limitations 13

Chapter 2 Publication 21
2.1 Introductory Abstract 21
2.2 Introduction 22
2.3 Background 23
2.3.1 Seismic History 25
2.4 Objective 26
2.5 Data 26
2.6 Methods 28
2.6.1 Filtering 28
2.6.2 Detections: No Picking Required 28
2.6.3 Associating Detections and Windowing Arrivals 29
2.6.4 Hypocenter Location 29
2.6.5 Error Reporting 31
2.6.6 Magnitude and Polarity 32
2.7 Results 32
2.7.1 Event Population Statistics 33
2.8 Discussion 35
2.9 Conclusion 37

Chapter 3 Getting Started with REST 49
3.1 Dependencies 49
3.2 Repository Organization 50
3.3 Running the Examples 51
3.3.1 Original Distribution 51
3.3.2 Modified version 52
3.4 Data Analysis Scripts 53
3.4.1 Time, Depth, and Magnitude Recurrence 53
3.4.2 Plotting 54
3.5 Parameter Modification 54
3.6 Future Modifications and Capabilities 55
3.7 Computational Limitations 56
3.7.1 Aftershock Sequences 56
3.8 Future Studies 57

Bibliography 58

Appendix A Station Information 67

Appendix B Supplemental Figures 72

LIST OF TABLES

A.1 Study region seismograph information 66

LIST OF FIGURES

1.1 Seismograph station map and study region 16
1.2 Generalized basemap of the Yakutat indentor and nearby features 17
1.3 Geologic setting of the Canadian Cordillera 18
1.4 ComCat-NEDB catalog of earthquakes from August 2016 – August 2018 19
1.5 Schematic drawing of a typical MMEP seismometer setup 20

2.1 Seismograph station map and study region 39
2.2 Generalized basemap of the Yakutat indentor and nearby features 40
2.3 Geologic setting of the Canadian Cordillera 41
2.4 ComCat-NEDB catalog of earthquakes tfrom August 2016 – August 2018 42
2.5 Local event spectrogram for 13 October 2016 M 4.1 earthquake 43
2.6 Full *REST* catalog of earthquake locations 44
2.7 Catalog comparison 45
2.8 Heatmap of earthquake locations from the *REST* catalog 46
2.9 Picked phase arrivals displayed in the program Gphase. 47
2.10 Moment tensor solutions for the Mackenzie Mountains 48

B.1 Event depths from the *REST* catalog 71
B.2 RMS residuals for each event from the *REST* catalog 72
B.3 Azimuthal gap (in degrees) from the *REST* catalog 73
B.4 Spatial and temporal differences in matching events 74

Chapter 1

Introduction and Background

Chapter 1 provides background information for the overarching field project and research methodology of this thesis. Topics of discussion include the geologic setting of the study region, context for the geological and societal significance of this project, logistical specifics and motivation for the Mackenzie Mountains EarthScope Project (MMEP), and the methodology and workflow used to obtain experimental results.

First, relevant historical and present tectonic and geodynamic processes affecting modern stress field interpretations will be discussed. Additional context will be presented describing the history of the MMEP seismometer deployment – a multi-year, international and collaborative project of groundbreaking scope and interest. The basic theory and methodology of this particular earthquake detection and location software is then introduced. The results and implications thereof will be discussed predominately in Chapter 2.

1.1 Geologic Setting

The region of interest for this study lies in northwestern Canada at the interface of the northern Canadian Cordillera and the stable Archean Slave Craton of the North American interior (Figure 1.1). Therein lie the Mackenzie Mountains, an arcuate fold and thrust belt roughly trending along the political boundary of the Yukon and Northwest Territories regions of Canada. The relevant large-scale tectonic history of the broader southeast Alaskan and northern Cordilleran region is bookended by the complex collision of allochthonous terranes during the Mesozoic or early Cenozoic, and by present deformation associated with the Yakutat indentor in the Gulf of Alaska (Figure 1.2) (Coney et al., 1980; Bruns, 1983; Marechal et al., 2015). Additional allocthonous terranes exist outboard of the Mackenzie Mountains, emplaced by either plate tectonic drift – resulting in sutured terranes – or through the accommodation of large-scale strike-slip movement, characteristic of the terranes adjacent to the Tinitina and Denali faults (Johnston, 2001). Dex-

tral offset of the Tintina fault alone is approximately 420 km between the lower Paleozoic and Cretaceous; aggregate regional offset of the Tintina, Denali, and Teslin-Thibert fault systems is approximately 800 km (Figure 1.3) (Roddick, 1967; Nelson et al., 2013b). These dislocations and collisions have resulted in complex crustal structure.

The regional geology of the Canadian Cordillera and cratonic interior can be broadly described by four morphogeological belts comprised of groups of terranes with similar paleogeographic history (Figure 1.3), two continent-scale, dextral strike-slip faults (the Tintina and Denali Faults), and active orogenesis throughout the Mackenzie Mountains (proposed by this study) and at the interface of the Canadian Cordillera and Archean craton of the Slave Province (Johnston, 2001; Nelson et al., 2013a). Morphogeological terranes are expressed as belts of tectonic provinces with a variety of origins. A northeast-southwest cross-section of the northern Canadian Cordillera reveals a broad trend of Proterozoic and ancestral North American terranes progressing to Cenozoic accretionary terranes, as well as the near present-day superposition of local magmatic provinces (Nelson and Colpron, 2007). Regional deformation of the Chugach–St. Elias Mountains is driven by the collision of the Yakutat block, an oceanic plateau with accreted mélange sediments, subducting obliquely beneath the North American plate in the Gulf of Alaska (Figure 1.2) (Worthington et al., 2012). Most of the differential plate motion between the Pacific and North America plates has been accommodated since the Pliocene by the Denali, Totschunda, and Queen Charlotte-Fairweather fault systems (Figure 1.2) (Richter and Matson Jr, 1971).

The cause of the ongoing Mackenzie Mountains uplift, at such a great distance from a plate boundary, remains uncertain. Various hypotheses exist which attempt to resolve the mechanisms of present convergence in the Mackenzie Mountains. The orogenic float hypothesis of Oldow et al. (1990) entails a basal detachment of the lower crust over which the upper and mid-crust is translated - displaced by a boundary force on one edge. This mechanical detachment would theoretically allow far-field strain transfer of the more rigid upper crustal sheet, as the detachment surface provides little resistance. A rigid backstop would represent the terminus of strain transfer, requiring accommodation to occur at the intersection of the weak and strong upper crustal layers,

or in a lateral zone of weakness (such as previously faulted rock) within the upper crust of the weak layer. Mazzotti and Hyndman (2002) present regional evidence and a 2D thermo-mechanical model describing circumstances for orogenic float in which a hot, weak lower crust has facilitated a lower crustal décollement, allowing strain transfer from the Yakutat indentor northeast across the Canadian Cordillera. Their hypothesis involves strain accommodation in the Mackenzie Mountains – a region of previous deformation and readily reactivated thrust faults.

The basal tractions hypothesis of Finzel et al. (2015) posits that tractions on the base of the lithosphere produce large-scale convergence across the region. In their models, asthenospheric flow is being deflected by the subducted portion of the Yakutat indentor partially into the western Cordillera and slowing as it reaches the Mackenzie Mountains. This energy transfer is assumed to be partially expressed as lithospheric thickening and convergence across the Cordillera (Ghosh et al., 2019). Further, a weak lower crust or crustal detachment is not required to satisfy this hypothesis, as is the case in Mazzotti and Hyndman (2002).

The cause of convergence and uplift in the Mackenzie Mountains from approximately 33 – 20 Ma is explored by Enkelmann et al. (2019) through thermochronology. The opening of the North Atlantic to the far northeast is viewed as a potential reactivator of previous regional deformation on the eastern front of the Mackenzie Mountains. However, no thermochronological cooling phase is identified in conjunction with the present episode of uplift and erosion in the region. This is interpreted as an indication that uplift only recently began, or simply that an adequate population of thermochronological samples has not yet been collected for study.

Heat flow in the Northern Cordillera is generally very high – indicative of thin and weak lithosphere (Lewis et al., 2003). This contrasts sharply with the cold and strong lithosphere of the neighboring Slave craton of the North American interior (Hyndman and Lewis, 1999; Russell et al., 2001). This strong lateral temperature and velocity heterogeneity introduces additional challenges for earthquake location, further discussed in Chapter 2 Section 2.6.4. Cordilleran crust is estimated to be uniformly thin – approximately 33 km – with high temperatures on the order of 800 – 1000° C at the Moho (Hyndman, 2017; Audet et al., 2019). Elastic thickness, T_e, is often

used as a first-order proxy for depth to the brittle-ductile transition zone – the depth beyond which the deformation regime shifts from brittle failure to non-localized plastic flow (Hyndman et al., 2009; Rutter, 1986). In the weak Cordilleran crust, Flück et al. (2003) resolves T_e at 20 – 40 km in the Cordillera and 100 km in the Craton. These values inform depth-limit assumptions in this study, discussed further in Chapter 2 Section 2.6.4.

1.2 Seismic Background

Present seismicity records indicate relatively high regional activity across the Mackenzie Mountains as well as in the Richardson Mountains to the north (Hyndman et al., 2005b). Faults in this region, such as the Plateau and Iverson thrusts (Figure 1.4), are thought to accommodate a large proportion of the regional strain, and could lead to a possible M_X 7.5 – 8.0 earthquake, resulting in high seismic hazard in the broader region (Gabrielse, 1991). To date, the largest known earthquake in the Yukon and Northwest Territories is the M_W 6.9 Nahanni earthquake of 1985 (Figure 1.4), which resulted in comprehensive modifications to the Canadian National Building Code (Hyndman et al., 2005a). In recent years, researchers have developed an active interest in studying the Alaska-Yukon region. Well-constrained seismicity in nearby regions (such as the Aleutian trench and along the Denali fault) and present deformation and orogenesis at the Cordillera-Craton interface (Freymueller and Woodward, 2013) highlight the relatively unknown seismic characteristics of the Mackenzie Mountains region. Additionally, the Alaskan and British Columbia coastline is highly seismogenic, with large M_W 6.2 and 6.3 earthquakes and accompanying aftershocks rupturing near Skagway, AK during the MMEP deployment alone (U.S. Geological Survey [USGS] Advanced National Seismic System Comprehensive Earthquake Catalog [ANSS ComCat] system, https://earthquake.usgs.gov/ [last accessed March 2020]). A regional seismicity map which combines the catalogs of the USGS ComCat and the Natural Resources Canada National Earthquake DataBase (NEDB) is shown in Figure 1.4 (Natural Resources Canada, 2019).

The Gutenberg-Richter relationship (Equation 1.1) describes the theoretical distribution of earthquakes above a specified value of completeness (Gutenberg and Richter, 1944),

$$\log_{10} N = a - bM. \tag{1.1}$$

Here, N is the total number of earthquakes with magnitude greater than M, a is the productivity value, and b (commonly referred to as the *b*-value) describes the relative proportion of large to small earthquakes in the study region. *b*-value calculations are an important consideration for seismic hazard analyses since they bear on the probability of larger earthquakes. Further, the *b*-value shows a negative correlation both with differential stress in continental interiors and with increasing depth (Scholz, 2015; Spada et al., 2013). The *b*-value is not strongly controlled by rock heterogeneity, as once thought (e.g., Mori and Abercrombie, 1997). Scholz (2015) shows that regions with normal faulting regimes correlate with the highest *b*-values relative to other fault types, thrust regimes have the lowest *b*-values, and strike-slip regions are likely to host intermediate *b*-values. In this study, *b*-values are calculated in accordance with the methodology derived by Aki (1965) and further described in Cao and Gao (2002). A Maximum Likelihood Estimate (MLE) is calculated for increasing cutoff magnitudes in accordance with the relationship described in Equation 1.2,

$$\hat{b} = \frac{\log_{10} e}{\bar{m} - (m_{\text{min}} - \Delta m/2)}, \tag{1.2}$$

in which $\hat{b}$ is the estimated *b*-value, e is Euler's number, m_{min} is the cut-off magnitude, $\bar{m}$ is the average magnitude of all earthquakes cataloged above the cut-off magnitude, and $\Delta m/2$ is half the binning width of the initial catalog. This method is preferred to a simple least squares regression because it assumes a Poissonian distribution of events, and downweights the importance of large-magnitude earthquakes which may be under or oversampled in the study period. A least squares regression would provide a biased estimate of the *b*-value and is thus inadvisable.

Little information about event source parameters is available in the study region. Limitations including sparsely distributed instrumentation and few larger-magnitude events have historically hampered the computation of centroid moment-tensor solutions (CMTs) in the Mackenzie Mountains region (Ristau, 2004). Kao et al. (2012) review and compute CMTs in accordance with the methodology described in Aki and Richards (1980) using improved parameterization for localized

regions in the Northern Cordillera. CMTs are determined for most earthquakes above M ∼3.4 - 3.7 in their study. CMT solutions indicate a dominant thrust faulting regime throughout the Mackenzie Mountains, which migrates to primarily transpressional or strike-slip faulting in the Richardson Mountains to the north. Generally, large events are rare in the craton region adjacent to the Cordillera.

1.3 MMEP Experiment

Researchers from Colorado State University, the University of Alaska, and Yukon College initiated the MMEP Experiment in July 2015 following the approval of the National Science Foundation – EarthScrope grant EAR-1460533. Alpine elevations, weather conditions, remote deployment locations, and a large study area all contributed to the pioneering nature of the project. For more information regarding the instrumentation and logistics of the MMEP, the reader is referred to Baker et al. (2020).

1.3.1 Project Motivation

Broadly, research goals for the MMEP involve building a better understanding of the Northern Canadian Cordillera region through the deployment of remote seismic instrumentation and geodesy. Specific topics of interest include understanding the causes of deformation of the Mackenzie Mountains, constraining the likely presence of a slab window, investigating lithosphere-scale tectonic structures, and imaging asthenospheric flow. Included in this mission are studies utilizing techniques for teleseismic and ambient noise tomography, mantle anisotropy, seismic source location, and geodesy.

Seismicity in the Mackenzie Mountains is understudied. Historically, this is due to the sparse distribution of seismographs in the region (Hyndman et al., 2005a). Lower-magnitude earthquakes can be observed and located with higher certainty as a result of the improved spatial density of a seismic array. A lack of properly resolved regional hazards maps, as well as an under-prepared local population (e.g., Hyndman et al., 2005a), can result in a heightened level of risk even for

moderate earthquakes. This study yields a higher resolution catalog of local earthquakes, thereby providing insight to the seismicity along active faults and diffuse seismicity within the Mackenzie Mountains.

1.3.2 Instrumentation

This experiment was supported by the Incorporated Research Institutions for Seismology (IRIS) Portable Array Seismic Studies of the Continental Lithosphere (PASSCAL) Instrument Center, from whom the instrumentation was loaned. The IRIS PASSCAL program is the result of a community-based effort to provide otherwise prohibitively expensive instrumentation and training to the staff of seismic research projects.

A schematic drawing of a typical MMEP seismic station is depicted in Figure 1.5. Güralp CMG-3T seismometers continuously recorded ground motion at 1, 40, and 100 Hz frequencies, with response corners at 120 s and 100 Hz. A Kinemetrics Quanterra Q330 data logger temporarily stored the data, which were transferred to the long-term storage Quanterra PB14F low temperature baler every 4 hours. The instrumentation was electrically powered via two sources, one primarily used in generally sunny conditions (typically from April to September), and the other used intermittently in dark or snow-covered conditions (October to March). The winter system was powered by a series of Cegasa zinc air cell batteries, ideal for low current and high voltage output even in very cold temperatures (rated to approximately -20°C). In sunny conditions, a 12 V heavy-duty lead acid battery was recharged via two 12 V solar panels, which were connected to the data logger through a power converter and stabilizer for consistent power output. The instrumentation was contained within two separate apparatuses; the seismometer was housed on a pedestal in an upside down trash can (i.e., a positive-pressure bell jar – typical only of the Yukon-side deployment), and the remaining electronics and batteries were housed in a Rubbermaid ActionPacker approximately 3 m away. The seismometer was leveled on a cement pedestal at the bottom of a buried vault, then aligned with true north. The ActionPacker was outfitted with a small wooden pedestal to elevate the Q330 in the event of minor flooding, and was otherwise sealed shut with weatherstripping. A

hole was drilled for wiring the solar panel and the seismometer to the data logger. This small hole was sealed with a weatherproof cover and steel wool to prevent small rodents from entering the housing.

1.3.3 Deployment

The deployment, servicing, and demobilization of seismometers was logistically complicated due to a number of factors. Instrument and supplies shipment timing, staging facilities, physical labor, and technical instrument installation were coordinated by members of the science party each field season. The MMEP was unique in that without prior information regarding sub-arctic, alpine deployments, new methods were necessarily developed and tested, often through trial-and-error. For more information regarding the logistics of deployment and recommended improvements for similar future projects, please see Baker et al. (2020).

The instrument deployment was staged in two legs – one originating in Whitehorse, YK, and the other in Norman Wells, NWT (herein referred to as the Yukon and NWT staging areas). The Yukon staging crew was equipped with two four-wheel-drive trucks, a 6 m flatbed trailer, and (in the demobilization stage) an ATV. Most Yukon stations were accessible via the Canol Road (used in decades past as a petroleum transport route), which ran along stations MM07 to MM27 (Figure 1.1). However, in the Northwest Territories the road is no longer maintained and is presently inaccessible. As such, the NWT staging area was chosen for its accommodation of chartered float plane and fixed gear flights, primarily by North-Wright Airways. The stations were primarily deployed on the northern shore of remote alpine lakes for maximum exposure to sunlight, and easy access and identification via float plane. Two stations (MM29 and MM32) were located adjacent to dirt runways and one station (MM33) was located adjacent to a barren field atop a ridge line used as a landing strip.

In July 2015, the MMEP experiment officially began with the deployment of four pilot seismograph stations: MM04, MM05, MM06, and MM27. In the following summer (2016), two teams of researchers deployed the remainder of the temporary array of seismometers over a roughly 875

km transect straddling the Mackenzie Mountains (Figure 1.1), filling in considerable space left by other networks. MM37 was not deployed due to an inundated deployment site, and MM01 – MM03 were not deployed due to permitting issues with the government of British Columbia. In summer 2017, with permitting issues resolved, MM01 – MM03 were deployed, as well as an additional station, MM41 (located in the substantial gap between MM27 and MM28). Recording at a broadband range of frequencies, the seismographs were deployed at these various intervals from June 2015 until August 2018, at which time all but three stations (MM14, MM22, and MM27) were demobilized.

1.3.4 Servicing

Seismic stations were necessarily serviced in the Northern Hemisphere summer months, approximately June through early September. Software upgrades, battery replacement, data collection, and station monitoring were required each year. When staging from the NWT, the Pilatus PC-6 Porter aircraft, outfitted with floats, was primarily utilized for access to seismometer sites located on small lakes in the Mackenzie Mountains. The de Havilland Canada DHC-6 Twin Otter was additionally employed for seismometer sites with earthen runways. The planes were flown by sight, with limited assistance from navigational instrumentation. Sub-arctic latitudes, combined with high elevation and rugged terrain, necessitated nearly cloudless, calm-wind conditions in order for the planes to safely travel to the stations.

Travel from the Yukon had a higher tolerance for bad weather, but was nonetheless dangerous given the propensity for sporadic summer storms and exposure to lightning. During servicing, data were retrieved via the baler (i.e., long-term storage "hard drive"), and field notes were recorded regarding various operational aspects of the station's operation. Any damage found at a station was assessed and repaired to working order, or, in rare cases, the station damage was deemed beyond repair and the station prematurely demobilized. To minimize the potential for the latter scenario, sufficient backup equipment was brought along to effectively rebuild every element of a temporary station, if necessary.

Deployment, servicing, and demobilization operations from both the Yukon and NWT staging areas required considerable attention to the dangers of site remoteness (necessitating mechanical autonomy, survival gear, and injury-free excursions) and the possibility of interactions with bears and moose.

1.3.5 Demobilization

In August 2018, the seismic array was demobilized with the exception of 3 stations – MM14, MM22, and MM27 – for which additional funding was secured. In prior years, some stations were demobilized early due to unforeseen circumstances. In 2017, MM08 was demobilized because of flooding, and MM31 due to a catastrophic bear attack. The process of demobilization involved data offload and retrieval, locking the seismometer (to prevent the sensitive weights from jostling during flight), and stowage of the equipment for transport. Once retrieved, the equipment was stored at its nearest staging facility and prepped for shipment. Each instrument, electronic device, and cable was cleaned, inventoried, and packed in its appropriate shipping container. The instrumentation was then shipped from its respective staging location back to the IRIS PASSCAL Instrument Center. Customs paperwork and approval was handled by IRIS.

1.3.6 Downtime

A notable amount of damage occurred to various instrumentation over the course of the deployment. Typical categories of damage include flooding, vandalism, cold-weather downtime, and interactions with bears (likely black or grizzly bears). However, without game cameras or other methods of verification, it was sometimes difficult to discern the cause of a particular type of damage. Certain patterns were generally observed for the different categories of damage. For example, bears would typically rip the tarps covering the ActionPacker, whereas vandals would release the cargo straps and remove the tarp without ripping the material. It is therefore surmised that bear damage was exclusive to the NWT leg (stations MM30, MM34, MM35, MM36, and MM39), and human-caused damage exclusive to the Yukon leg (stations MM07, MM20, and MM21). For more

information regarding the bear-related damage experienced by the Mackenzie Mountains network and others, the reader is referred to Baker et al. (2020) and Tape et al. (2019).

The issue of flooding was discovered during the first years' servicing, at which time it was observed that spring snow melt had inundated several of the ActionPackers (MM08, MM15, MM25, MM26, and MM38). They were then reburied at a slightly shallower depth, to position the lid of the ActionPacker above the ground. Cold-weather outages were observed following Q330 temperature readings of approximately -6° C – such as at stations MM06, MM15, MM28, MM30, MM34, MM39, and MM40 – despite an expected low-temperature rating of -20° C. Those stations became operational once again when temperatures rose.

In total, approximately 91% of the potential data were successfully retrieved for the MMEP. Approximately 5% of the total downtime was caused by bears, with the other 95% attributed to flooding, vandalism, cold-weather outages, and erroneous wiring. We consider this a highly successful deployment and in the future recommend the use of electrical fencing or highly engineered enclosures for protection from bear encounters (Tape et al., 2019). Additional recommendations include precautions for flooding (i.e., siting in well-draining soil, lip of ActionPacker above ground) and potentially better-insulated instrument enclosures.

1.4 Earthquake Detection Methodology

The novelty of this particular study is derived from both newly collected data (of the MMEP) as well as the utilization of software – herein referred to as *REST* (Recursive Estimator) – which nearly completely automates the process of earthquake location and catalog generation. Ordinarily, earthquake detection requires an analyst to manually "pick" phase onset times, scrub the data for dead or otherwise empty digital files of recorded ground motion (these recordings are often referred to as a seismic "trace"), and perform a variety of other time-intensive and skilled-labor tasks. This software package requires relatively few user-defined inputs and only the execution of a single script to accomplish – with a high level of accuracy – the same task. Rawles and Thurber (2015) report an approximately 95% agreement in phase onset estimation between skilled

earthquake analysts and the method adapted for use in the *REST* software. With the proper parameterization, one can confidently detect and locate earthquakes using only raw seismic traces and several specification files. The software package requires few dependencies and utilizes (with slight modification) a tractable amount of computational power for an average workstation.

1.4.1 General Theory

Earthquake detection and location is a longstanding field in seismology of significant importance to the public. Since the early 1960s it has been used as a means of nuclear treaty verification regarding adherence to non-proliferation agreements (Pomeroy et al., 1982). At short time-scales (on the order of tens of seconds), rapid earthquake location and magnitude estimation can help provide an early warning to those populations vulnerable to intense shaking after the initial rupture of an earthquake (e.g., Wald et al., 2011). Locating earthquakes is additionally useful in determining the hazards associated with seismic activity by constraining fault locations and slip rates, informing local tomographic models, assessing the seismogenic nature of a particular region for geotechnical or engineering purposes, and for earthquake forecasting (e.g., Cornell, 1968; Wiemer and Schorlemmer, 2007). In particular, this catalog is used to determine upon which faults displacement is actively occurring. The results of this study can inform hazards models with an improved, higher-resolution earthquake catalog.

In this project, automatic earthquake detection software is employed to generate a catalog of events – herein referred to as the *REST* catalog – during the MMEP deployment period. The methodology is described as follows, in the order of execution of the processing steps. In general, the algorithms begin with more lenient parameters, detecting very small perturbations and attempting to locate somewhat unlikely events. These constraints become increasingly selective as the workflow progresses. This is done to ensure the capture of all potential events, however unlikely at first, because it is nearly impossible to identify them later in the workflow. All data begin as three-channel raw seismic traces (i.e., data are recorded with specific sensitivity to vertical, north-south, and east-west oriented motion) for any number of stations located within the study

region. For the specific methodology utilized in each of the processing steps, the user is referred to Chapter 2 Section 2.6.

1.4.2 Experimental Workflow

REST (a series of programs written in C and FORTRAN) works in 8 steps, which are herein grouped and referred to as *Stage One* (of two) of the catalog generation. For more information on the specifics of the processing, please see Chapter 3. *Stage One* begins by downloading and filtering raw seismic traces, followed by initializing the appropriate directories and parameter files contained therein. Next, the data processing stages (described in Chapter 2 Section 2.6) are implemented via the *REST* code. The software implements a sensitive signal detection algorithm over the time series data and associates those detections across the array as potential events. Seismic traces are subsequently windowed about estimated event arrival times. The location algorithms begin to iteratively solve for a best-fit solution of the location and time of the earthquake, followed by magnitude and polarity estimates. Lastly, results are stored in a master catalog file.

Whereas *Stage One* is nearly fully automated, *Stage Two* consists of a suite of scripts tailored to the needs of the particular user for data analysis. The final catalog from *Stage One* should be post-processed to remove low-confidence events or false detections. Analyses performed on the resultant catalog can include *a*- and *b*-value calculations, magnitude of completeness determinations, and frequency-recurrence and depth-recurrence histograms. Spatial, magnitude, and statistical relationship plots, and as well as detection comparison heatmaps can also be generated. For more information on each of these analyses, please reference Chapter 3.

1.4.3 Limitations

Certain computational and experimental limitations exist within the parameters of this study. Computational limitations primarily include run time and memory requirements. Experimental limitations include a sparse station distribution relative to the study region size, which impacts our ability to catalog aftershock sequences or small events. Without adequate station spacing and minimal azimuthal gap, earthquake locations will have increased uncertainty.

Run Time

REST utilizes significant processing power and random access memory (RAM) during certain stages of computation, often in excess of modern workstations. Particularly during the windowing phase of the workflow, Seismic Analysis Code (SAC) files are loaded into memory and windowed appropriately. For example, for large datasets of 5-day SAC files (which in our study would consist of 339 potential traces, each approximately 66.7 MB), memory requirements for the windowing phase can exceed 22 GB for each windowed event (of which there are sometimes thousands). This amount of RAM is intractable for most personal workstations. In an effort to reduce the total run-time and memory requirements, several instances of the software are manually run in parallel over relatively smaller (3-day) windows of data at a time, utilizing only approximately 13 GB of RAM.

Spatial Resolution

The sub-linear array of seismographs of the MMEP spanned nearly 900 km across the Canadian Cordillera. Despite the existence of several auxiliary networks in the study region (e.g. TA, CN, etc.) (Figure 1.1), the geometry of the MMEP array and sparse availability of other stations often does not provide ideal azimuthal coverage for locating earthquakes. Additionally, the typical problem of depth constraint for hypocenters still exists with this method of earthquake location. This is because changes in source depth do not have a straightforward trade-off with origin time. Using an S-wave detection from even just one station (provided that station is with 1.4 focal depth's distance) can dramatically improve depth estimation, as it provides more information about the lateral heterogeneity and geometry of the model region (Gomberg et al., 1990). However, this threshold is easily surpassed given the sparse distribution of seismic stations relative to the study region size.

Our large study region introduces additional complications regarding both overlapping and small events. Overlapping events (i.e., the last arrivals of the first event are still reaching far-away stations when a new event begins) are much more likely to occur given the large spatial distribution of stations. In absolute time, for example, phase arrivals can be identified at opposite ends of a seismic network only seconds apart, ultimately resulting in an undetermined location. Additionally, small earthquakes can often be difficult to locate when obscured by the coda from

other large events (even if the events are not overlapping). The effects of attenuation and low signal-to-noise ratios often require employing specialized techniques for event location.

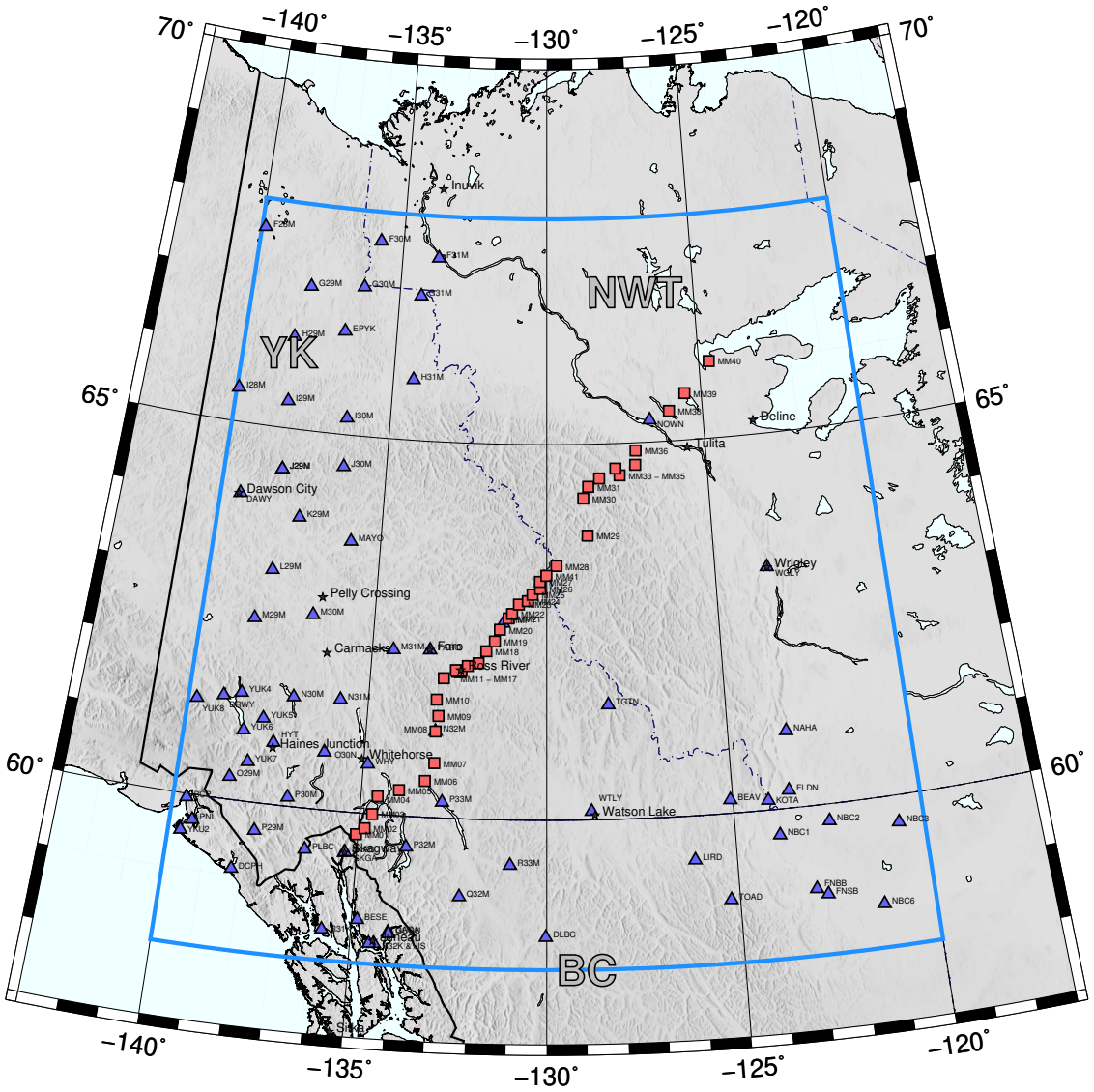

Figure 1.1: Seismograph station map and study region. The Mackenzie Mountain seismograph array (red squares) trends northeast along a sub-linear array over approximately 875 km. Temporary and permanent stations (blue triangles) during the two-year deployment are additionally shown. The blue box represents the extent of the study area. The Canol Road (not shown) runs along MM07 to MM27.

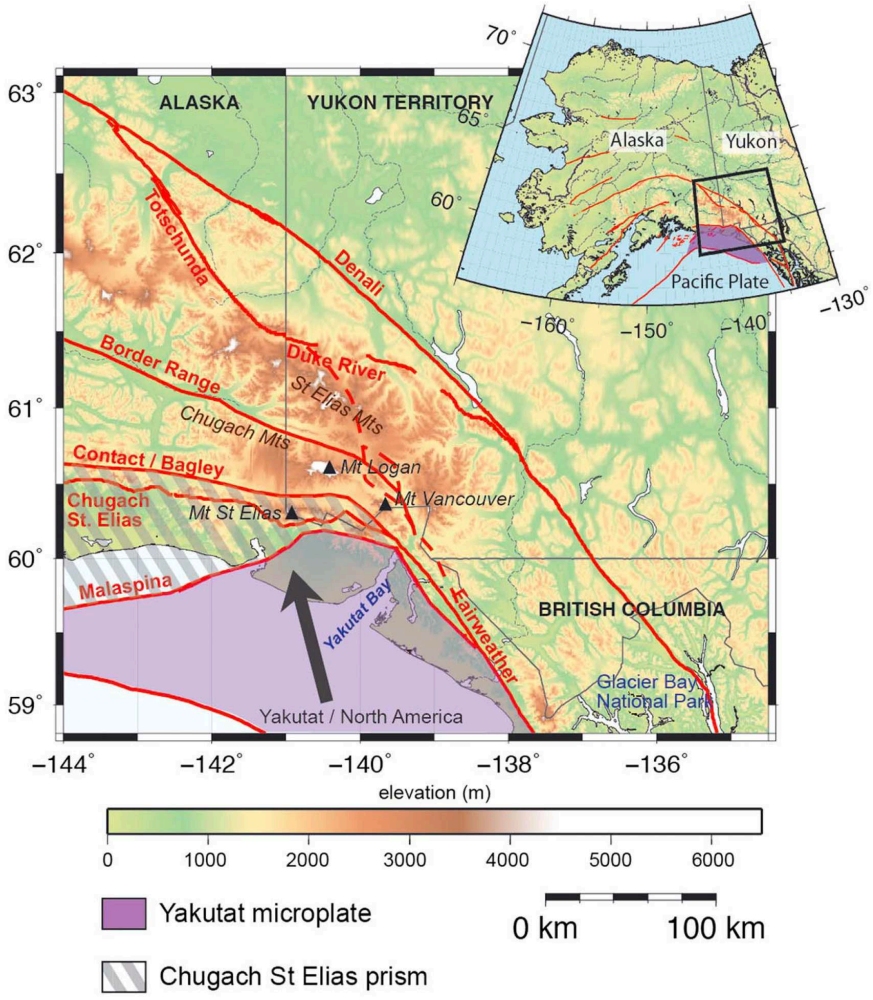

Figure 1.2: Map of the Yakutat indentor (modified from Marechal et al. (2015)). Red lines indicate faults, black triangles are volcanoes, and the arrow shows the direction of convergence of the Yakutat indentor with North America.

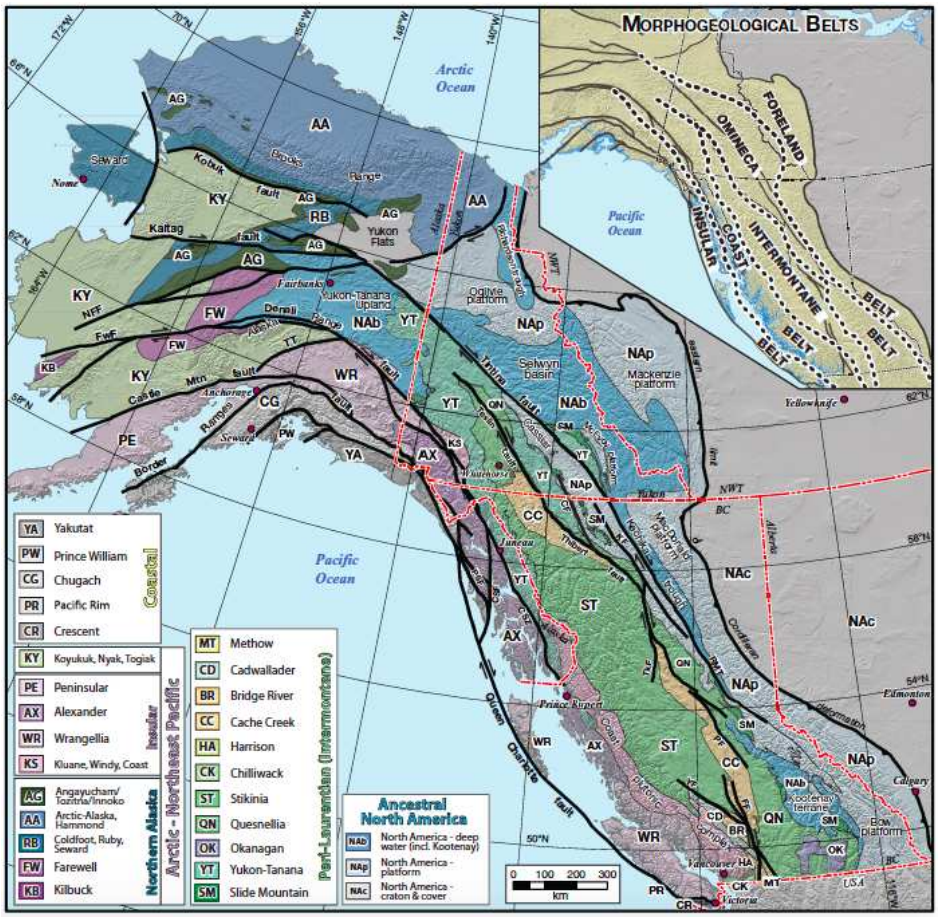

Figure 1.3: Geologic setting of the Canadian Cordillera (modified from Nelson et al. (2013a)). Morphogeologic belts (grouped by paleogeography) and terranes of the Northern Cordillera. The study area is largely comprised of the Ancestral North American and Peri-Laurentian terranes. Label NAc is the North American Craton; contained therein is the Slave Craton.

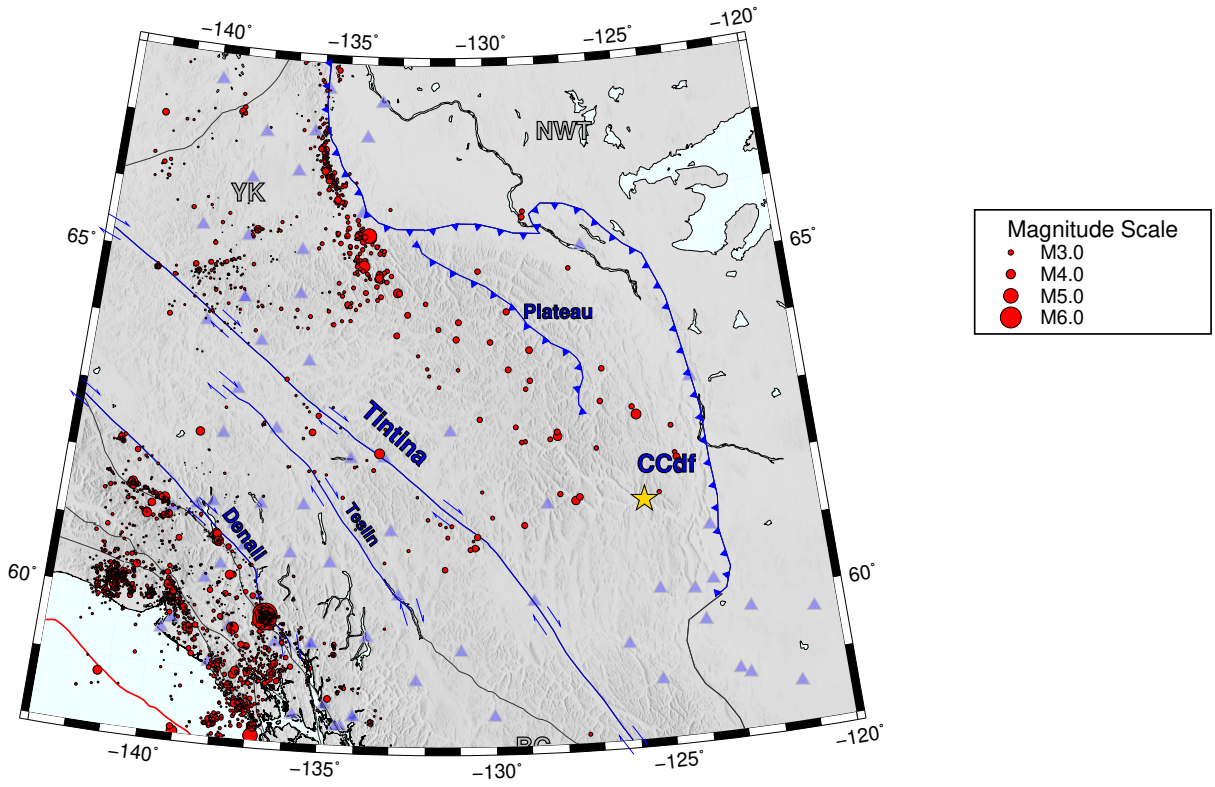

Figure 1.4: M $\geq$ 0.5 earthquakes from August 2016 to August 2018 detected in the Northern Cordillera (red circles), retrieved from the ANSS ComCat and NEDB web services. Hypocenters are scaled to magnitude. Blue lines running generally NW to SE represent major faults in the region – the Tintina, the Teslin, Denali, and Plateau faults, and the eastern extent of the Canadian Cordillera deformation front (CCdf). The 1985 M_W 6.9 Nahanni earthquake is labeled with a gold star for historical reference. Faint blue triangles are the broadband seismic stations which were operational during the study period.

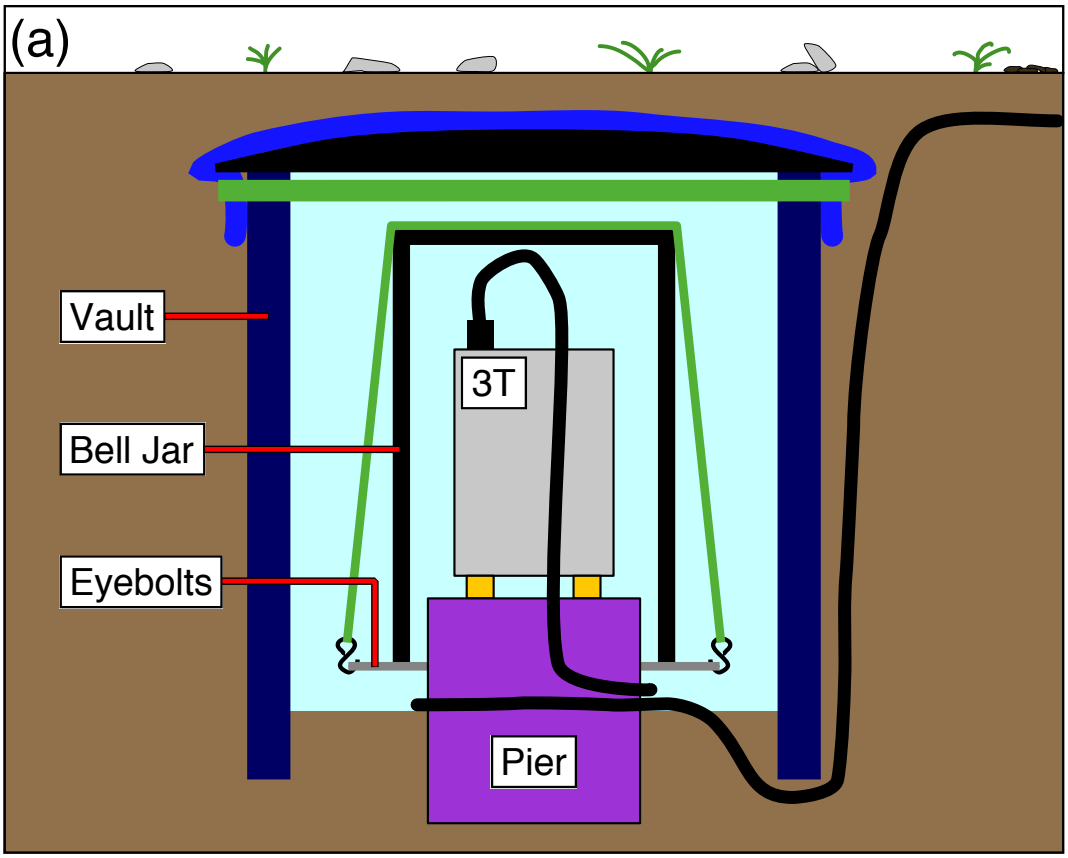

Figure 1.5: Schematic drawing of a seismometer housed in a vault, for a typical seismic station deployed in the MMEP (modified from Baker et al. (2020)). Bell jars were only utilized for the Yukon-side deployment.

Chapter 2

Publication

This chapter is the draft of a manuscript for publication in the Seismological Society of America's *Seismological Research Letters*. The results and interpretations discussed herein are preliminary and subject to change.

2.1 Introductory Abstract

The Mackenzie Mountains are an actively uplifting and seismogenic arcuate thrust belt lying within the Northwest Territories and Yukon, Canada. Seismic activity in the region is poorly constrained due to a historically sparse seismograph distribution. In this study, new data are analyzed from the 40-station, ~875 km-long Mackenzie Mountains temporary network (Baker et al., 2020) crossing the Cordillera-Craton region adjacent to and within the Mackenzie Mountains, in conjunction with Transportable Array and other sparsely distributed arrays in the region. Data from approximately August 2016 – August 2018 are processed and compared to the sparse-network earthquake catalog records maintained by the USGS and Natural Resources Canada. Using algorithms developed by Kushnir et al. (1990), Rawles and Thurber (2015), and Roecker et al. (2006), signals are identified and subsequently associated across the network to note potential events, estimate phase onsets, and resolve hypocenter locations. This study improves the regional earthquake catalog by detecting smaller-magnitude earthquakes and lowering the regional magnitude of completeness from M_c = 2.5 to 1.9. Within the Mackenzie Mountains and immediately surrounding areas we find 524 new events and additionally recommend an updated location for 185 previously cataloged events. Our *b*-value computation for the updated catalog (0.916 ± 0.08) likely indicates a relatively high level of regional differential stress. We identify the spatial distribution of earthquakes in the Mackenzie Mountains as diffuse, and offer far-field stress transfer as a mechanism for producing widespread reverse faulting observed in the region. Further, we associate regional

seismicity with tectonic activity in the context of known faults and orogenic provinces such as the Richardson Mountains.

2.2 Introduction

Earthquake detection and location is a longstanding field in seismology of significant importance to the public. Since the early 1960s it has been used as a means of nuclear treaty verification regarding adherence to non-proliferation agreements (Pomeroy et al., 1982). Engineering specifications for large-scale infrastructure – such as oil pipelines or commercial buildings – often include special consideration for seismic hazards (Finn, 2000). At time-scales on the order of tens of seconds, rapid earthquake location and magnitude estimation can help provide an early warning to those populations vulnerable to intense shaking after the initial rupture of an earthquake (e.g., Wald et al., 2011). Locating earthquakes is additionally useful in determining the hazards associated with seismic activity by constraining fault locations and slip rates, informing local tomographic models, assessing the seismogenic nature of a particular region for geotechnical or engineering purposes, and for earthquake forecasting (e.g., Cornell, 1968; Wiemer and Schorlemmer, 2007).

In this study, new data are analyzed from the 40-station, ~875 km-long Mackenzie Mountains EarthScope Project (MMEP) temporary network (Baker et al., 2020) crossing the Cordillera-Craton region adjacent to and within the Mackenzie Mountains of Yukon and Northwest Territories, Canada, in conjunction with Transportable Array and other sparsely distributed stations in the region. Stations from the MMEP fill in considerable coverage gaps left by other temporary and permanent networks in the region (Figure 2.1). Data from approximately August 2016 – August 2018 are processed and compared to the sparse-network earthquake catalog records maintained by the U.S. Geological Survey (USGS) and Natural Resources Canada. We present a new, higher-resolution earthquake catalog for the Mackenzie Mountains and surrounding regions, and offer subsequent recommendations for additions and modifications to regional earthquake catalogs. This new catalog is statistically compared to existing catalogs, and the new locations interpreted in terms of regional seismicity.

2.3 Background

The study region lies in northwestern Canada at the interface of the northern Canadian Cordillera and the stable Archean Slave Craton of the North American interior (Figure 2.1). A primary target is the seismogenic Mackenzie Mountains, an arcuate fold and thrust belt trending roughly along the political boundary of the Yukon and Northwest Territories regions of Canada. The relevant large-scale tectonic history of the broader southeast Alaskan and northern Cordilleran region is book-ended by the complex collision of allochthonous terranes during the Mesozoic or early Cenozoic, and by present deformation associated with the Yakutat indentor in the Gulf of Alaska (Figure 2.2) (Coney et al., 1980; Bruns, 1983; Marechal et al., 2015). Those allochthonous terranes primarily exist outboard of the Mackenzie Mountains, emplaced by either plate tectonic drift – resulting in sutured terranes – or through the accommodation of large-scale strike-slip movement, characteristic of the terranes adjacent to the Tinitina and Denali faults (Johnston, 2001). Dextral offset of the Tintina fault alone is approximately 420 km between the lower Paleozoic and Cretaceous; aggregate regional offset of the Tintina, Denali, and Teslin-Thibert fault systems is approximately 800 km (Figure 2.3) (Roddick, 1967; Nelson et al., 2013b). These dislocations and collisions have resulted in complex crustal structure.

The regional geology of the Canadian Cordillera and cratonic interior can be broadly described by four morphogeological belts comprised of groups of terranes with similar paleogeographic history (Figure 2.3), two continent-scale, dextral strike-slip faults (the Tintina and Denali Faults), and active orogenesis throughout the Mackenzie Mountains (proposed by this study) and at the interface of the Canadian Cordillera and Archean craton of the Slave Province (Johnston, 2001; Nelson et al., 2013a). Regional deformation of the Chugach–St. Elias Mountains is driven by the collision of the Yakutat block, an oceanic plateau with accreted mélange sediments, subducting obliquely beneath the North American plate in the Gulf of Alaska (Figure 2.2) (Worthington et al., 2012). Most of the differential plate motion between the Pacific and North America plates has been accommodated by the Denali, Totschunda, and Queen Charlotte-Fairweather fault systems since the Pliocene (Figure 2.2) (Richter and Matson Jr, 1971).

The cause of the ongoing Mackenzie Mountains uplift, at an unusually far distance from a plate boundary, remains uncertain. Various hypotheses exist which attempt to resolve the mechanisms of present convergence in the Mackenzie Mountains. The orogenic float hypothesis of Oldow et al. (1990) entails a basal detachment of the lower crust over which the upper and mid-crust is translated - displaced by a boundary force on one edge. This mechanical detachment would theoretically allow far-field strain transfer of the more rigid upper crustal sheet, as the detachment surface provides little resistance. A rigid backstop would represent the terminus of strain transfer, requiring accommodation to occur at the intersection of the weak and strong upper crustal layers, or in a lateral zone of weakness (such as previously faulted rock) within the upper crust of the weak layer. Mazzotti and Hyndman (2002) present regional evidence and a 2D thermo-mechanical model describing circumstances for orogenic float in which a hot, weak lower crust has facilitated a lower crustal décollement, allowing strain transfer from the Yakutat indentor northeast across the Canadian Cordillera. Their hypothesis involves strain accommodation in the Mackenzie Mountains – a region of previous deformation and readily reactivated thrust faults.

The basal tractions hypothesis of Finzel et al. (2015) posits that tractions on the base of the lithosphere produce large-scale convergence across the region. In their models, asthenospheric flow is being partially deflected by the subducted portion of the Yakutat indentor into the western Cordillera and slowing as it reaches the Mackenzie Mountains. This slowing is expressed as lithospheric thickening and convergence across the Cordillera (Ghosh et al., 2019). Further, a weak lower crust or crustal detachment is not required to satisfy this hypothesis, as is the case in Mazzotti and Hyndman (2002).

The cause of the second most recent episode of convergence and uplift in the Mackenzie Mountains (from approximately 33 – 20 Ma) is explored by Enkelmann et al. (2019) through thermochronology. The opening of the North Atlantic to the far northeast is viewed as a potential reactivator of previous regional deformation on the eastern front of the Mackenzie Mountains. However, no thermochronological cooling phase is identified in conjunction with the present episode of uplift and erosion in the region. This is interpreted as an indication that uplift only re-

cently began, or simply that an adequate population of relevant thermochronological samples has not yet been collected for analysis.

2.3.1 Seismic History

Present seismicity records indicate relatively high regional activity at the southern end of the Mackenzie Mountains as well as in the Richardson Mountains to the north (Hyndman et al., 2005b). Faults in this region, such as the Plateau and Iverson thrusts (Figure 2.4), are thought to accommodate much of the regional strain, and could lead to a possible magnitude 7.5 – 8.0 earthquake, resulting in high seismic hazard for the broader region (Gabrielse, 1991). To date, the largest recorded earthquake in the Yukon and Northwest Territories is the M_W 6.9 Nahanni earthquake of 1985 (Figure 2.4), which resulted in comprehensive modifications to the Canadian National Building Code (Hyndman et al., 2005a; Adams and Atkinson, 2003). In recent years, researchers have developed an interest in the Alaska-Yukon region, noting well-constrained seismicity in nearby regions (such as the Aleutian trench) and present deformation and orogenesis at the Cordillera-Craton interface (Freymueller and Woodward, 2013). The Alaskan and British Columbia coastline is highly seismogenic, with large M_W 6.2 and 6.3 earthquakes and accompanying aftershocks rupturing near Skagway, AK during the MMEP deployment alone (USGS Advanced National Seismic System Comprehensive Earthquake Catalog [ANSS ComCat] system, https://earthquake.usgs.gov/ [last accessed March 2020]). A regional seismicity map which combines the catalogs of the USGS ComCat and the Natural Resources Canada National Earthquake DataBase (NEDB, http://earthquakescanada.nrcan.gc.ca/stndon/NEDB-BNDS/bulletin-en.php [last accessed March 2020]) is shown in Figure 2.4 (Natural Resources Canada, 2019). These reported earthquake catalogs provide a basis for which new catalogs can be compared against to check for similar detections of larger events, and help target expectations for the highest concentration of regional seismicity.

2.4 Objective

Earthquake location estimation helps to constrain the locations of active faults. Identifying the regions associated with active deformation can lead to information about the present nature of geologic activity in the region. Fault locations also provide vital information to community planning boards, commercial developers, pipeline manufacturers, and individuals seeking to minimize their risk of experiencing a hazardous seismic event. The objectives of this study are to locate and robustly catalog small, previously unrecorded earthquakes in the area, and to constrain the location and nature of active regional faults.

2.5 Data

Newly available data from the MMEP are recorded by a temporary array of seismographs deployed in the Yukon and Northwest Territories, Canada, from approximately August 2016 to August 2018. In total, 40 seismographs were deployed along a northeasterly-trending path spanning from near Whitehorse, BC, Canada, across the Mackenzie Mountains and into the stable craton, terminating at Great Bear Lake. For more information regarding the MMEP, the reader is referred to Baker et al. (2020). Additional public data from the Transportable Array and other sparsely distributed stations (network identifiers CN, AK, PN, PO, AT, NY, YO, and ZQ) are jointly analyzed over the same time period. In total, 113 stations are utilized in this experiment. Due to animal damage to the stations, mechanical malfunctions, and anthropogenic interactions with the stations, rarely are data from all 113 seismometers available for a given time period. Rather, stations were individually repaired, redeployed, or demobilized at various times throughout the duration of this study. For a full list of seismograph station locations used in this study, please see Appendix A.

Local earthquakes dominate the 1 to 10 Hz passband, but can produce significant energy at frequencies above 10 Hz, sometimes to 30 Hz (Figure 2.5). Sampling frequency requirements for this catalog are thus satisfied by broadband recording channels (BHZ, BHE, and BHN), which are typically sampled at 40 Hz. Certain stations record high frequency channels only – these data

were decimated during the web request from the Incorporated Research Institutions for Seismology (IRIS) Data Management Center (DMC).

The velocity model used in this study is a 1D combination of values from Ma and Audet (2017) and Schaeffer and Lebedev (2014). The Ma-Audet model describes crustal velocities in the study region to a depth of 30 km, and the Schaeffer-Lebedev model provides a broader regional average of velocities from 30 km depth to 400 km depth (the maximum depth of the model). Cordilleran crust is estimated to be uniformly thin (approximately 33 km) with high temperatures on the order of 800 – 1000° C at the Moho (Hyndman, 2017; Audet et al., 2019). Elastic thickness, T_e, is often used as a first-order proxy for depth to the brittle-ductile transition zone – the depth beyond which the deformation regime shifts from brittle failure to non-localized plastic flow (Hyndman et al., 2009; Rutter, 1986; Smith and Bruhn, 1984). In the weak Cordilleran crust, elastic thickness is modeled at approximately 20 – 40 km, in comparison with $\sim$100 km in the Slave Craton (Flück et al., 2003). For this reason, the *REST* software is parameterized to prefer locating hypocenters above 30 km depth (to allow some room for error).

The USGS ANSS ComCat web service is queried for earthquakes identified in the study region from August 2016 – August 2018 for magnitudes greater than 0.5. Over 99% of the returned events are located by the Alaska Earthquake Center. Event magnitudes below 4.0 are typically calculated as a local, Richter-type magnitude (M_L), and events above or near magnitude 4.0 are typically moment magnitudes (M_W) or a subtype thereof (Hanks and Kanamori, 1979). Additionally, the Natural Resources Canada NEDB web service is queried for events using the same parameters as above. The catalogs are compared for "matching events" (defined here as events which occur within 30 km and 4 s of each other) and then combined. Matching events are cataloged with their ComCat estimation of location, time, magnitude, etc.

The fractal distribution of earthquake hypocenters about a mainshock, fault, or system of faults can make choosing a study region challenging. An initial, large study region from 140° W to 120° W and 58° N to 68° N is utilized for traveltime calculation and event location. However, a smaller region is later utilized to focus statistical characterization on those events occurring within

a closer proximity to the Mackenzie Mountains (and specifically the MMEP seismic array). The preferential region is bounded at 136° W to 120° W and 60° N to 68° N (Figure 2.1). In the initial, large region the *REST* catalog contains 4,578 events, and the combined ComCat-NEDB catalog contains 6,716 events, of which 2,831 events match (between the *REST* and ComCat-NEDB catalog). In the preferential region, these respective figures are reduced to 709 events in the *REST* catalog and 542 events in the matching ComCat-NEDB catalog, of which 185 events match.

2.6 Methods

An event catalog was constructed for the study region from roughly August 2016 – August 2018, for which the *REST* program was utilized (Roecker, unpublished). The data were processed in a mostly automated procedure of filtering, detection, windowing, onset and phase arrival estimation, and inversion for hypocenter location. Magnitude and polarity estimates were additionally calculated for each event we cataloged.

2.6.1 Filtering

The data were first filtered to reduce noise and enhance signals of interest to facilitate picking. For impulsive arrivals, acausal artifacts can be unintentionally introduced with certain filtering methods (e.g., Allam et al., 2014), resulting in an erroneous pick of the arrival time. A single-pass, four pole Bessel filter was utilized with consideration for preserving the onset time in the seismic trace.

2.6.2 Detections: No Picking Required

The signals were analyzed using a Bayesian statistical and finite dimensional parameterization approach described by Kushnir et al. (1990). The data were autocorrelated with specified lags across a single vertical channel for a seismic station. A quadratic form of the data was then computed and compared against a triggering threshold. In this approach, noise is characterized by taking the average of the entire time-series across a moving specified interval – typically about 1

hour for periods of quiet seismicity and 7 minutes for aftershock sequences. When the summation of the autocorrelation squares surpasses the pre-defined triggering threshold, that time in the seismic trace is recorded as a positive detection. An example of positive detections is shown in Figure 2.9. Note that an obvious phase arrival is not picked (station K29M). This is a trade-off of using an automatic detection algorithm. However, for our purposes there are enough other arrivals that are correctly picked to mitigate this shortcoming.

2.6.3 Associating Detections and Windowing Arrivals

A simple sorting algorithm is used in which temporally associated detections are grouped as a potential event. For example, a positive event group is created if a sufficient number of detections occur within a pre-defined time limit of one another (Here: 15 s). Controls on the minimum number of stations at which there is a positive detection, as well as the maximum time-spacing between detections, should be modified appropriately according to the geometry of the seismograph deployment and size of the region of interest.

Next, data are windowed around the potential phase arrivals for each seismogram. This operation is performed at all stations and channels to ensure the capture of any possibly useful information for locating an earthquake. Two user-specified values control the length of the windows. The first cuts each trace (in absolute time) a specified number of seconds prior to the first arrival in the event group, and the second specifies the number of seconds after the last arrival at which to cut the data.

2.6.4 Hypocenter Location

Finite difference solutions to the eikonal equation (Equation 2.1) – first introduced by Vidale (1990) – are found in accordance with the methodology described in Hole and Zelt (1995) and used to calculate traveltime tables:

$$\left(\frac{dt}{dx}\right)^2 + \left(\frac{dt}{dy}\right)^2 + \left(\frac{dt}{dz}\right)^2 = s^2(x, y, z). \tag{2.1}$$

Here, t is the travel time, x, y, and z the coordinate axes, and s is the ray slowness. Essentially, this grid-based method finds the steepest traveltime gradient between adjacent nodes for every location in a pre-defined velocity grid, and stores them in a traveltime library. The relationship described in Brocher (2005) is utilized to relate the V_P and V_S wavespeed models. Traveltime tables are calculated only once for the entire set of stations, and then appropriately referenced for each attempted event location. Therefore, events cannot be located outside of the initially calculated grid, and all seismographs must exist within the boundaries of the grid.

The iterative process of refining an event hypocenter is performed by finding the least-squares solution to the root mean square (RMS) reduction of the traveltime residuals. At most, the algorithm is permitted four rounds of misfit reduction. However, if it is apparent after any round that the misfit is too large (i.e., it is unlikely that the onset estimates come from a single true event), the algorithm moves on to the next potential event. The process begins with iterative onset estimation refinement based on the methodology described in Rawles and Thurber (2015). The data are effectively scored against a series of reference templates (with positive examples of P- and S-wave arrivals) using a nearest-neighbor approach developed by Nikolov (2012). Additional scoring is computed against negative templates (data containing only P-wave coda, or all zeros, for instance). A ratio curve is computed which identifies the maximum value of positive to negative template matches. This local maximum is chosen as the phase onset. This process effectively automates (with approximately 95% efficiency) the rigorous and sometimes difficult task of phase picking, commonly the most exhaustive task performed by earthquake analysts (Rawles and Thurber, 2015).

Event location is performed using methods similar to the *tomoFD* software described in Roecker et al. (2006). Location estimation uses a simple grid-based searching method (with reference to the earlier-computed traveltime tables) which attempts to minimize the variance in the misfit of the chosen hypocenter location and initiation time. The hypocenter is relocated in the updated model a maximum of four times before a location is determined and the updated model is discarded.

An additional challenge of earthquake location is resolving vertical depth. This is because variations in source depth do not have a straightforward effect on origin time. Using an S-wave

detection from even just one station (provided that distance to the station is within 1.4 times the focal depth) can dramatically improve depth estimation, as it provides more information about the lateral heterogeneity and geometry of the model region (Gomberg et al., 1990). However, this threshold is easily surpassed given the sparse distribution of seismic stations relative to the study region size. We note artificial depth reporting is widespread in both the *REST* and ComCat-NEDB catalogs. Bins at regular depth intervals often contain an anomalously high number of events due to hypocenter depths that were unchanged from a particular starting model. In the *REST* catalog, these artificial surfaces occur at approximately 2, 7, 12, and 17 km depths, and in the ComCat-NEDB catalog at 0, 5, and 12.5 km depths.

2.6.5 Error Reporting

Using the methodology described by Roecker et al. (2006), confidence intervals and probability density functions (PDFs) are readily calculated in accordance with Tarantola and Valette (1982). Assuming a Gaussian-distributed probability of hypocenter location, a triaxial error ellipsoid is computed for each event location by integrating the appropriate marginal PDF. The PDF itself is calculated in the final iteration of hypocenter location. This is a time-consuming operation, so it is performed at a coarser resolution than the actual location search. In other words, the reported error dimensions represent the maximum possible uncertainty in the location. Additionally, the standard deviation of the travel-time residuals is calculated. Both very high and low values could indicate an unlikely event, even in the final catalog. Care should be taken to cull such events, which sometimes do not get removed by other algorithms. Lastly, the average weight value is reported. The square root of the reciprocal of this value represents the average data uncertainty in seconds. Higher average weight values indicate more confident event locations. Presently, reported errors in the new catalog are not accurate, due to a dramatic underestimation of accumulated uncertainty in the wavepaths of a given earthquake. As a result, even a modest residual causes the location error estimation to plummet to zero.

2.6.6 Magnitude and Polarity

The final routines of the software involve performing magnitude and polarity estimations on the located events. Magnitude estimation is a simple Richter-type magnitude calculation, described in Equation 2.2:

$$M = a * [\log_{10}(A_{\text{max}})] + b * [\log_{10}(dt)] - c \tag{2.2}$$

in which M is the magnitude, A_{max} is the maximum amplitude of the P coda in a windowed portion of the event, and dt is the difference in the S and P arrival times. Values for a, b, and c are pre-defined constants. This simple calculation cannot be modified for site-specific amplification effects, and therefore often necessitates a correction via polynomial regression to the known magnitude distribution of a prior catalog.

The polarity estimate aims to determine whether, upon the P-wave arrival, the first-motion at a station was compressional or dilatational. A simple algorithm calculates the direction of first motion between the first and second zero-crossings.

Additional calculations include the ratio of the amplitude of the first arrival to the prior background noise (a simple signal-to-noise ratio), the event-station distance, event back azimuth, and the azimuthal gap (largest space between stations used in a detection, in degrees) for a particular event. The RMS of the residuals for a given event are also reported, along with triaxial error ellipsoid dimension for event locations, and the number of phases (P, S, and total) used to detect a given event.

2.7 Results

We cull events from our catalog using statistical output from the *REST* software, as well as fidelity comparisons against matching events in the ComCat-NEDB combined catalog. Events with RMS residuals higher than 1.5 s are removed, as well as events with high uncertainty. Events with very high or very low standard deviations, or events with improbable P and S phase arrival counts (e.g., a M_L 1.0 event with 30+ P arrivals, or an event with 25 P arrivals and no S arrivals) were additionally culled, as those are indicators of unlikely events. We regress our catalog of

matching events (those events that occur within 30 km and 4 s of a ComCat-NEDB event) and find a moderate negative correlation (R^2 = 0.41) with azimuthal coverage. We interpret this to suggest large azimuthal gap as an indication of poorly located events, and as a result cull events with a greater than 180° gap in coverage (at which point the recalculated regression presents an R^2 value of 0.029). We additionally cull events outside of our focus region (136° W to 120° W and 60° N to 68° N) for this particular study.

2.7.1 Event Population Statistics

The Gutenberg-Richter relationship (Equation 2.3) describes the theoretical distribution of earthquakes above a specified value of completeness (Gutenberg and Richter, 1944),

$$\log_{10} N = a - bM. \tag{2.3}$$

Here, N is the total number of earthquakes with magnitude greater than M, a is the productivity value, and b (commonly referred to as the *b*-value) describes the relative proportion of large to small earthquakes in the study region. *b*-value calculations are an important consideration for seismic hazard analyses since they bear on the probability of larger earthquakes. Further, the *b*-value shows a negative correlation both with differential stress in continental interiors and with increasing depth (Scholz, 2015; Spada et al., 2013). The *b*-value is not strongly controlled by rock heterogeneity, as once thought (e.g., Mori and Abercrombie, 1997). Scholz (2015) shows that regions with normal faulting regimes correlate with the highest *b*-values relative to other fault types. Thrust regimes have the lowest *b*-values, and strike-slip regions are likely to host intermediate *b*-values. We calculate *b*-values for the culled *REST* and ComCat-NEDB catalogs in accordance with the methodology derived by Aki (1965) and further described in Cao and Gao (2002). A Maximum Likelihood Estimate (MLE) is calculated for increasing cutoff magnitudes in accordance with the relationship described in Equation 2.4,

$$\hat{b} = \frac{\log_{10} e}{\bar{m} - (m_{\text{min}} - \Delta m/2)}, \tag{2.4}$$

in which $\hat{b}$ is the estimated *b*-value, e is Euler's number, m_{min} is the cut-off magnitude, $\bar{m}$ is the average magnitude of all earthquakes cataloged above the cut-off magnitude, and $\Delta m/2$ is half the binning width of the initial catalog. This method is preferred to a simple least squares regression because it assumes a Poissonian distribution of events, and downweights the importance of large-magnitude earthquakes (which may be under or oversampled in the study period). A least squares regression would provide a biased estimate of the *b*-value and is thus inadvisable.

Despite some artifical depth-binning in our hypocenter locations, we estimate the seismogenic zone to be distributed about approximately 12.5 km depth. We believe this is more tightly constrained than the COMCAT/NEDB counterpart catalog.

The *REST* software's magnitude calculation cannot be modified for region-specific (or network-specific) accuracy, so a transformation to the magnitude distribution of a professionally generated catalog is required. We accomplish this by regressing the magnitudes of "matching events" and modifying *REST* magnitudes appropriately. The *b*-value of our newly generated catalog (within our initial, large study region) is 0.891 $\pm$ 0.08. The *b*-value of the ComCat-NEDB catalog is 0.800 $\pm$ 0.05. In our focus region, *b*-value calculations are again performed and yield respective values of 0.916 $\pm$ 0.08 for the *REST* catalog and 1.128 $\pm$ 0.31 for the ComCat-NEDB catalog.

Magnitude of completeness (M_c) is defined as the magnitude above which 100% of the events in the study region are detected (Rydelek and Sacks, 1989). In our focused study region we identify 285 events above our M_c of 2.3 in the time period from August 2016 – August 2018, shown in Figure 2.6. Of the total events cataloged in this time period (not just those above the M_c), 185 have a counterpart present in the combined ComCat and NEDB catalog, and 524 are unique events. The ComCat-NEDB catalog contains 100 events above its M_c of 2.8. This represents a statistically tenuous quantity of events for *b*-value computation, as the recommended number of events for each catalog is greater than 2,000 (yielding a standard error of 0.05, or approximately 98% confidence intervals) (Aki, 1965).

In total, we record 143,641 P and 123,025 S phase arrival picks for located events. On average, matching events between the *REST* and ComCat-NEDB catalogs in the large study region differ in

location by 3.99 $\pm$ 3.86 km and in origin time by 0.5 $\pm$ 0.5 seconds. In the focused study region, these respective figures are 4.51 $\pm$ 4.23 km and 0.5 $\pm$ 0.5 s. The NEDB catalog does not report location errors, and the ComCat catalog only reports location errors for 9% of the total number of events. Earthquake recurrence in the study area is shown in Figure 2.7a, overlain by a plot of station availability. Depth recurrence is shown in Figure 2.7b, and a frequency-magnitude plot with the fitted log-linear Gutenberg-Richter relationship is plotted in Figure 2.7c. Figures of the azimuthal coverage, RMS of the event residuals, and average weight are included in Appendix A. Additionally, a "difference plot" is shown, which represents the difference in location and timing of *REST*-cataloged events to their ComCat-NEDB counterparts (where available).

2.8 Discussion

We note much improved resolution of small-magnitude events occurring within the Mackenzie Mountains in the *REST* catalog based on empirical calculations of M_c. Sampling bias related by proximity to the MMEP array is evident, as shown by the heatmap in Figure 2.8. Additionally, we note biased depth determinations for many events, evident by the artificially large bins at regular depth intervals in those histograms (Figure 2.7).

We observe broad seismicity across the Mackenzie Mountains and concentrated activity within the Richardson Mountains, which is indicative of a generally tectonically active region. Somewhat surprisingly, we do not find seismicity related to the 1985 Nahanni earthquake aftershock sequence. Seismicity is tightly focused in the Richardson Mountains, but diffuses outward as one moves south, with most earthquakes occurring in a belt southwest of the Plateau fault (Figure 2.6). Previous studies show that relative motion of the Northern Cordillera (from GPS measurements) is estimated at approximately 2.4 $\pm$ 1.3 mm/yr at N4°W $\pm$ 24° by Fletcher and Freymueller (2003) in reference to stable North America, and slightly faster at 4.5 $\pm$ 1.0 mm/yr in the direction of N20°E $\pm$ 10° in reference to Yellowknife, NWT by James et al. (2001) and Mazzotti and Hyndman (2002). Calculations of accommodation from regional seismicity by Leonard et al. (2008) yield a median shortening rate in the Mackenzie Mountains of approximately 1.8 – 3.9 mm/yr,

suggesting nearly all of the deformation in the Mackenzie Mountains is seismic (Hyndman et al., 2005b). Therefore, nearly all of the uplift in the Mackenzie Mountains is occurring to the southwest of the Plateau fault. Regional centroid-moment tensor solutions computed and summarized by Kao et al. (2012) (Figure 2.10) further support shortening, primarily through E-W oriented reverse faulting in the Mackenzie Mountains, proceeding to a N-S oriented transpressional system in the Richardson Mountains to the north. This suggests that the orientation of the deviatoric stress field in the region changes laterally, possibly as a result of interactions with the stable Slave Craton to the east, which – as a result of high elastic thickness relative to the weak Cordilleran crust – acts as a pinning structure about which deformation is deflected (Flück et al., 2003). Significant fold and thrust fault systems exist throughout the Mackenzie Mountains (Powell, 2017), which are known to readily reactivate at a lower Coulomb stress criterion than unfaulted rock, and are well-documented as the origin of much of the world's intraplate seismicity (Scholz, 1998; Sibson, 1990; Sykes, 1978). It therefore follows that large scale strain transfer (as proposed by both the Mazzotti and Hyndman (2002) and Finzel et al. (2015) hypotheses) is likely being accommodated across the Mackenzie Mountains range to the southwest of the Plateau fault by a series of reactivated late Cretaceous to early Tertiary faults.

We note a lack of clear seismic activity along the Tintina and Teslin faults. Despite approximately 420 km of historical slip along the Tintina fault alone, this dextral-slip, transpressional system is either dormant or has a recurrence interval outside of the sampling range of this study. This is in agreement with indications that most of the differential plate motion between the Pacific and North America plates has been accommodated by the Denali, Totschunda, and Queen Charlotte-Fairweather fault systems since the Pliocene. (Richter and Matson Jr, 1971).

The *b*-value inversely corresponds to the proportion of large to small events occurring in a region (e.g., Frohlich and Davis, 1993). Factors such as stress regime, material properties, pore pressure, and volcanic or hotspot activity can affect the *b*-value for a specific region (e.g., Mogi, 1962). However, recent work shows that the differential stress regime has a strong negative linear correlation with *b*-value (Scholz, 2015), and may in fact be the dominant control. Our low *b*-value

further supports the existence of a primarily thrust regime in the Mackenzie Mountains region, with implications for high differential stress relative to other generalized regions of either predominantly strike-slip or normal faulting regimes. The *b*-value in our study (0.916 ± 0.08) is similar to other thrust regimes around the world, such as those found in Turkey, Switzerland, and Japan (Scholz, 2015; Spada et al., 2013). The diffuse spatial distribution of events is additionally in agreement with other intraplate regions in the world such as the Himalayas, Brazilian plateau, and Zargos Mountains of Iran (Talwani, 1989; Rocha et al., 2016; Shoja-Taheri and Niazi, 1981).

Seismic hazard analyses fall outside of the scope of this study, and are not performed due to the small sample size of events in our preferred region. A more complete earthquake catalog – with perhaps two decades of data – would enable an accurate characterization of the hazards in this region. An under-prepared local population necessitates further study in the Yukon and Northwest Territories (e.g., Hyndman et al., 2005a). Additionally, the risks of intraplate earthquakes are often understated, due to lower attenuation compared to more active regions at plate margins (Nuttli, 1973).

We note several shortcomings of the automated cataloging method used in this study. The effects of noisy time periods (such as in an aftershock sequence) obscure the presence of low-magnitude events. Additionally, events which are overlapping (i.e., the last arrivals of the first event are still reaching far-away stations when a new event occurs) often result in no location determination. The velocity model used in this study was a 1D combination of the Ma and Audet (2017) and Schaeffer and Lebedev (2014) models, and does not account for the substantial lateral velocity variations in the Craton and Cordillera (Schutt et al., in preparation). A plot of the RMS residuals confirms this bias in the velocity model, wherein some regions are systematically better-fit than others (Appendix B).

2.9 Conclusion

Cataloging earthquakes is a crucial step in understanding active tectonic processes in the Mackenzie Mountains. Pipeline manufacturers, commercial developers, and first-responders benefit from

the knowledge of underlying seismic risk. Characterizing statistical properties of the *REST* catalog enables future interpretations of the seismic hazards associated with large-scale strain transfer across the Canadian Cordillera and Craton. We observe diffuse seismicity across the Mackenzie Mountains fold and thrust belt, consistent with intraplate regions undergoing large-scale strain transfer and accommodation (Talwani, 1989). Statistical metrics such as the a- and b-values of our cataloged events are additionally consistent with intraplate regions (e.g., Shoja-Taheri and Niazi, 1981).

We recommend 2,465 unique events be added to the USGS ComCat and Canadian National Earthquake DataBase catalogs, and additionally recommend relocating 1,560 previously cataloged events. Information from our *REST* catalog should be utilized for hazard analyses, such as in the Canadian National Seismic Hazard Maps (Halchuk et al., 2015). Ergodic site amplification, spectral acceleration, and other products should be computed for the region, synchronous with geologic and digital elevation maps for the region for adequate hazards modeling. Additionally, we recommend the use of advanced techniques for locating overlapping events and small-magnitude events obscured by noise other coda from other non-overlapping events.

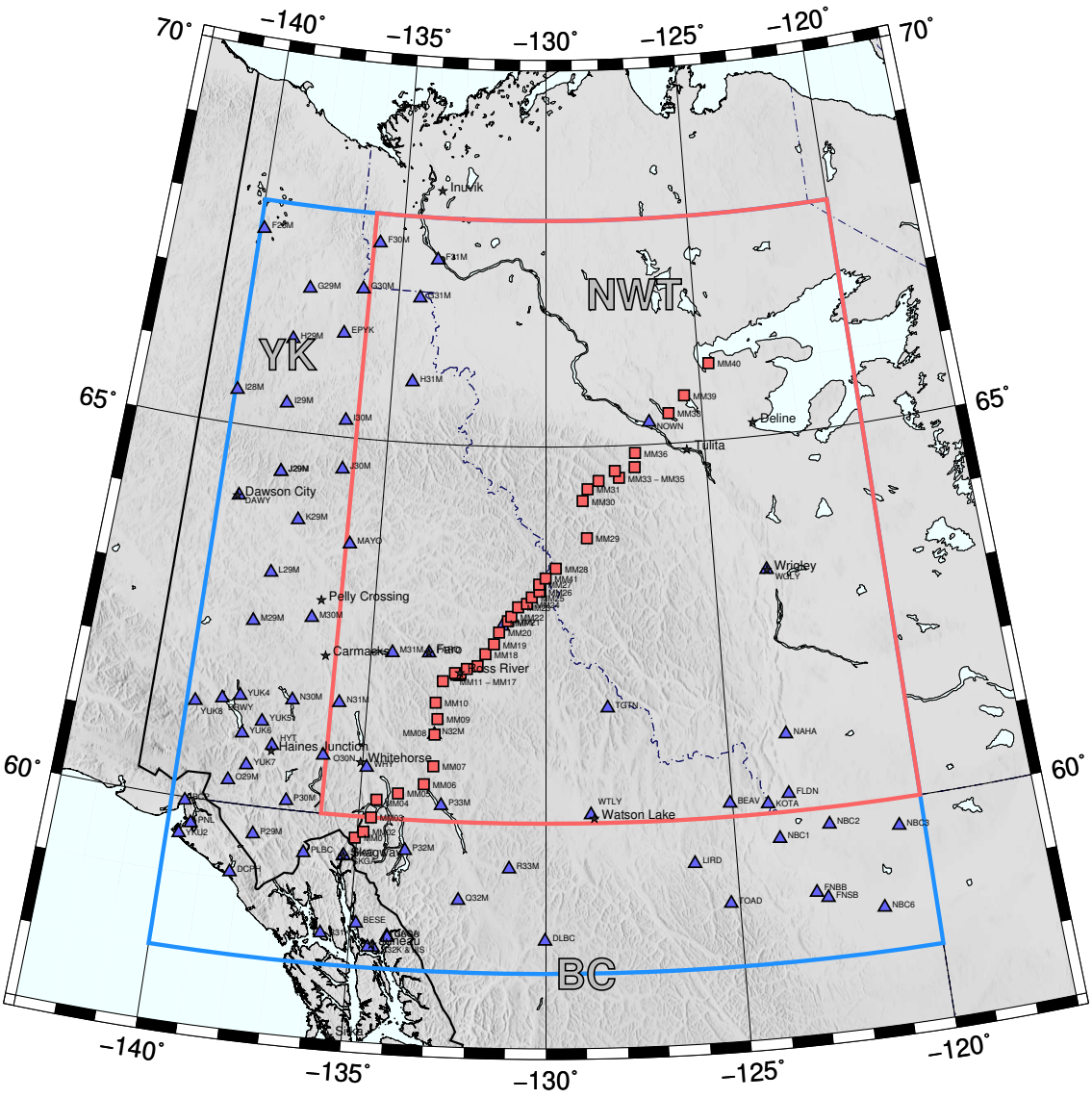

Figure 2.1: Seismograph station map and study region. The Mackenzie Mountain seismogram array (red squares) trends northeast along a sub-linear array over approximately 875 km. Other temporary and permanent stations (blue triangles) during the two-year deployment are additionally shown. The blue box is the extent of the study area and the red box is our focused study region. The Canol Road (not shown) runs along MM07 to MM27.

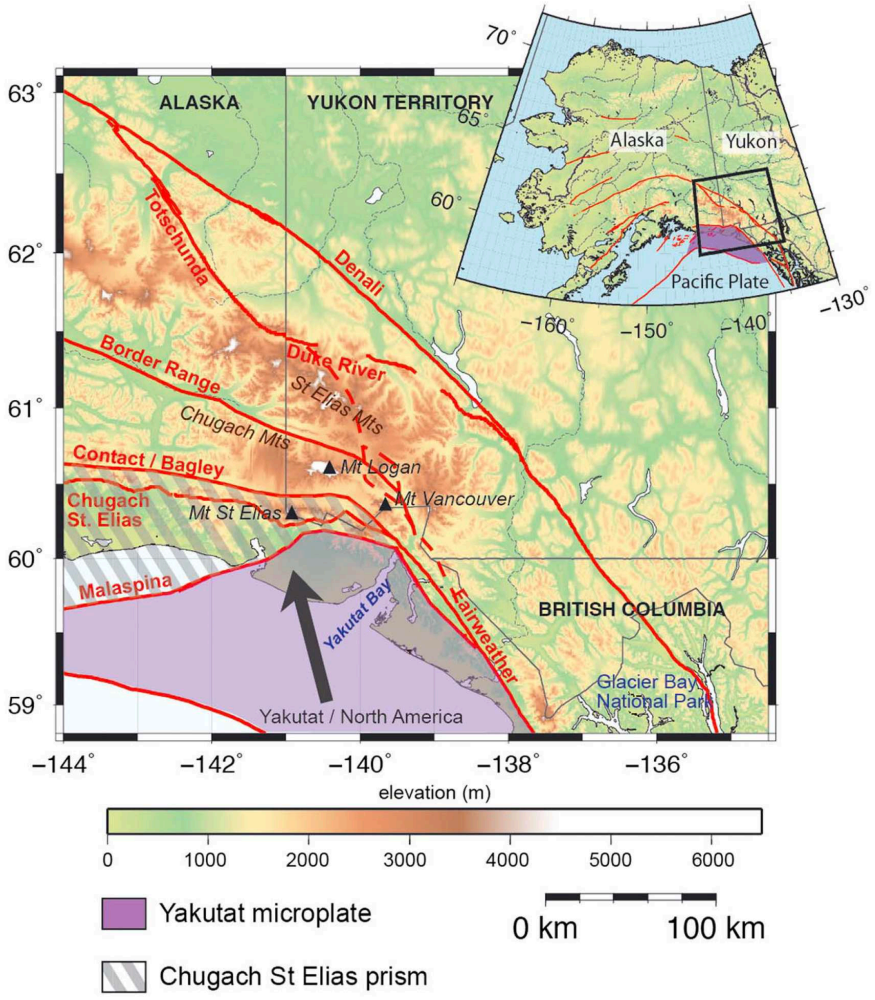

Figure 2.2: Basemap of the Yakutat indentor and nearby faults (modified from Marechal et al. (2015)). Cartoon basemap of the Yakutat indentor colliding with the St. Elias-Chugach Mountains. Also show are the Fairweather, Denali, and Totschunda faults.

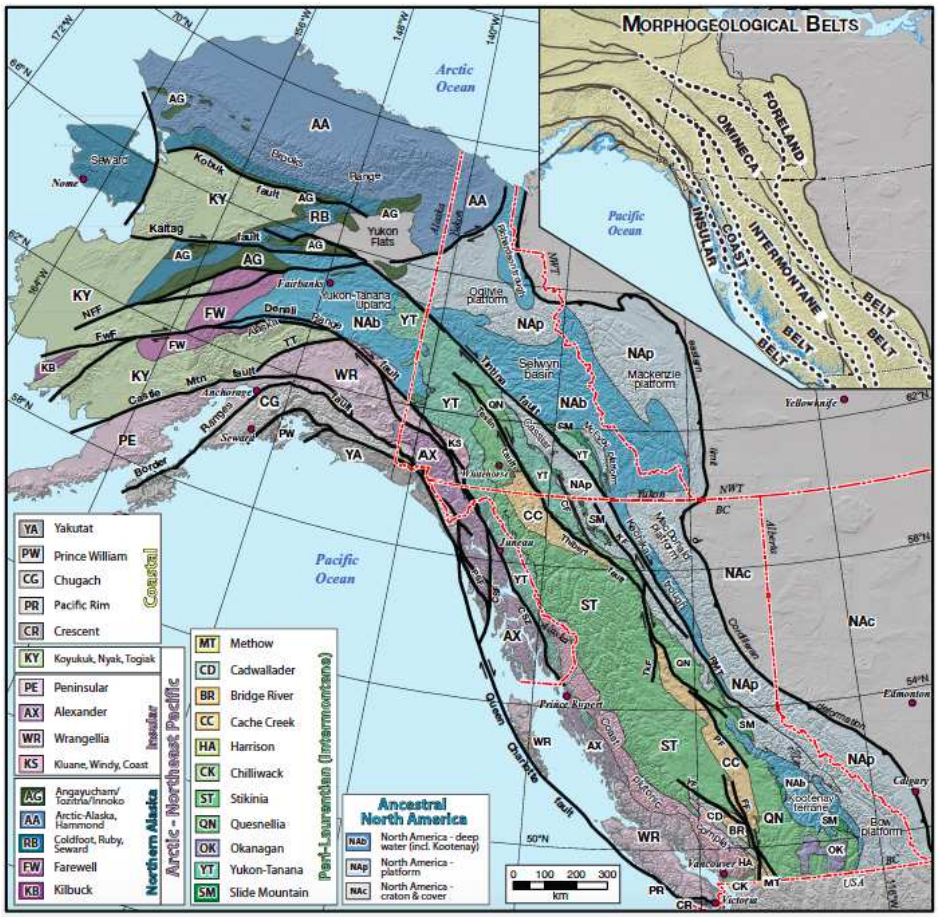

Figure 2.3: Geologic setting of the Canadian Cordillera (modified from Nelson et al. (2013a)). Morphogeologic belts (grouped by paleogeography) and terranes of the Northern Cordillera. The study area is largely comprised of the Ancestral North American and Peri-Laurentian terranes. Label NAc is the North American Craton; contained therein is the Slave Craton.

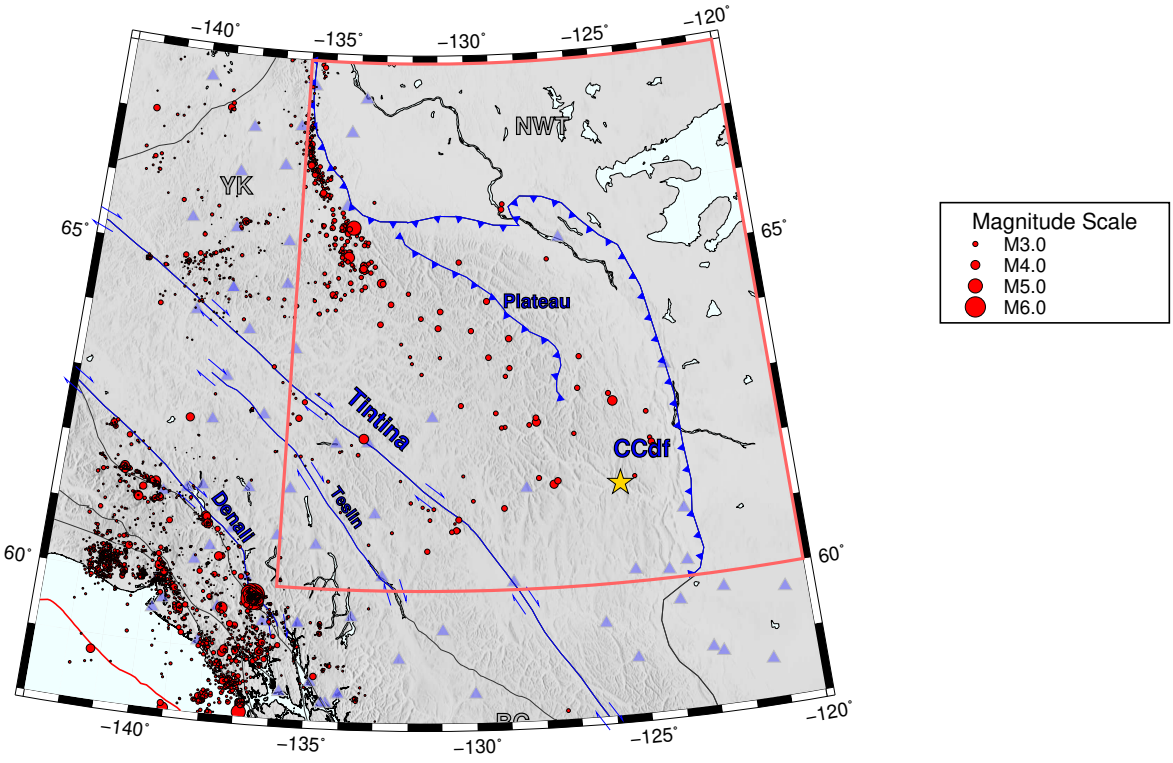

Figure 2.4: M $\geq$ 0.5 earthquakes from August 2016 to August 2018 detected in the Northern Cordillera (red circles scaled to magnitude) retrieved from the USGS ComCat and Natural Resources Canada NEDB web request services. Blue lines running generally NW to SE represent major faults in the region – the Tintina, the Teslin, Denali, and Plateau faults, and the eastern extent of the Canadian Cordillera deformation front (CCdf). The 1985 Nahanni earthquake is labeled with a gold star for historical reference. The red box is the extent of our focus region, used to closely analyze events primarily occurring within the Mackenzie Mountains. Faint blue triangles are the broadband seismic stations operating during the study period.

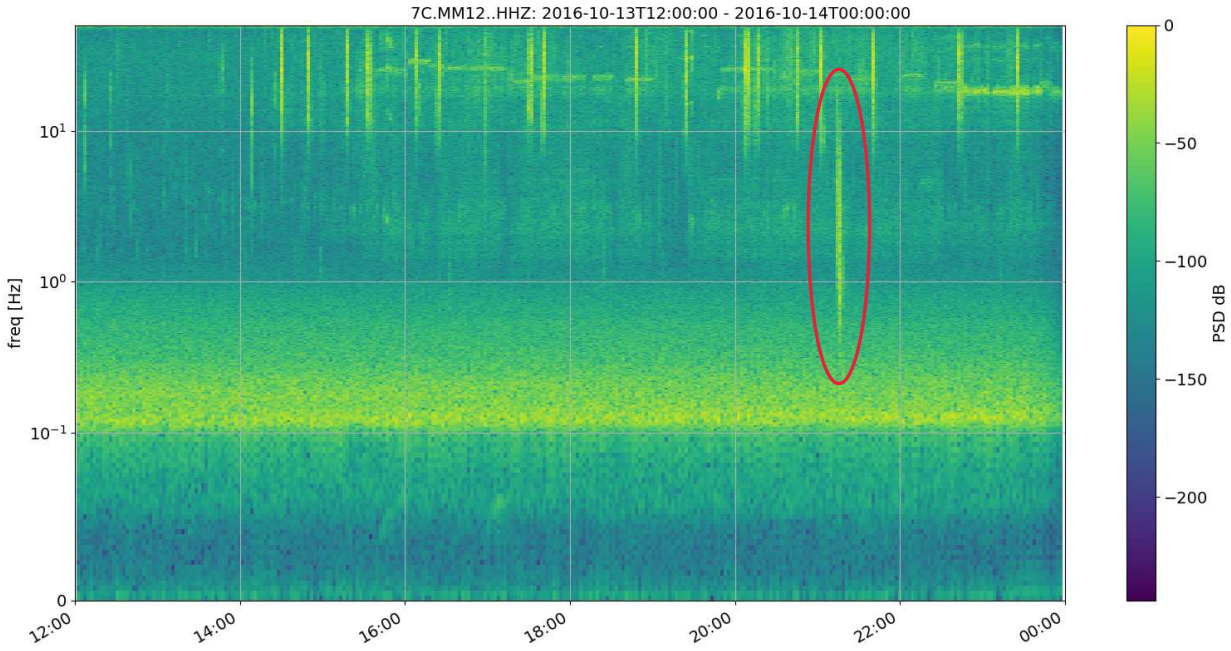

Figure 2.5: Spectrogram of a local M 4.1 earthquake on October 13, 2016 (circled by red oval). Energy from the event dominates the 1 - 10 Hz frequency range. This event (and other similar local events) are the basis for choosing the bandpass filter.

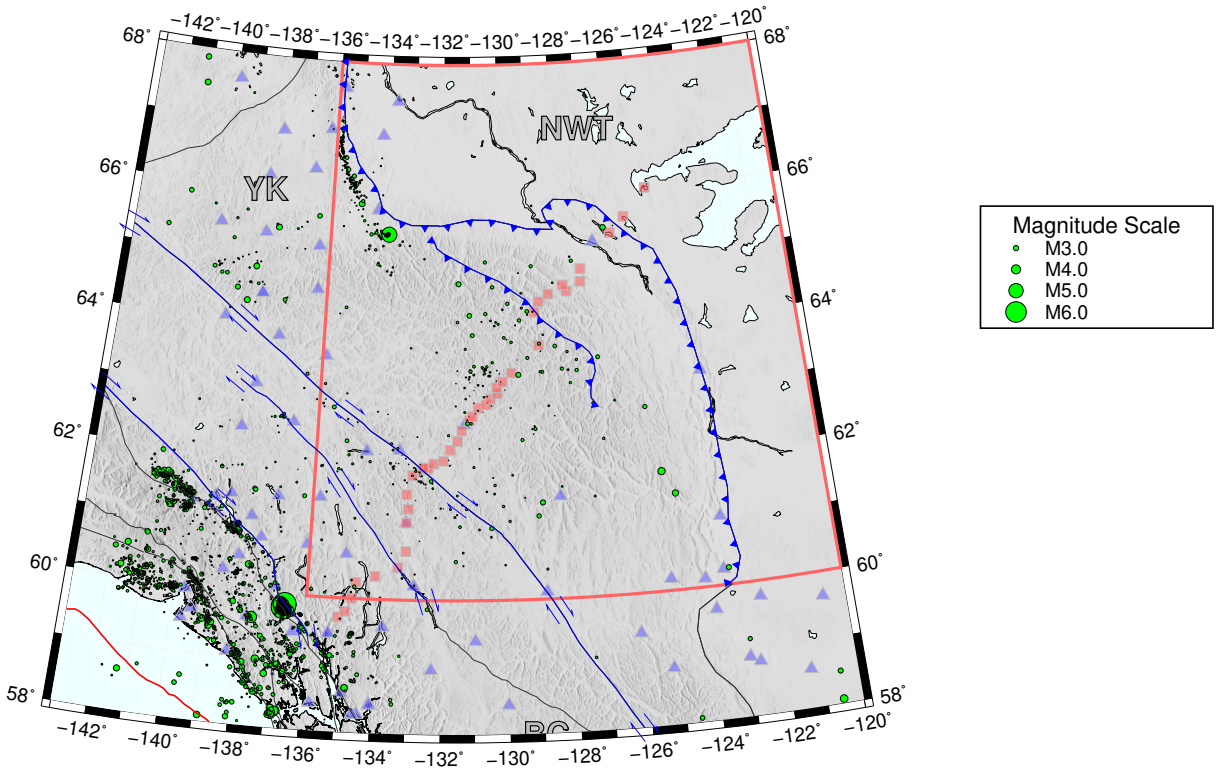

Figure 2.6: Full catalog of earthquake locations (green circles scaled by magnitude) generated using *REST*. The red box is the extent of our focus region, used to closely analyze events primarily occurring within the Mackenzie Mountains. Faint blue triangles and red squares are the broadband seismic stations of other seismic networks and the MMEP, respectively, which were operational during the study period.

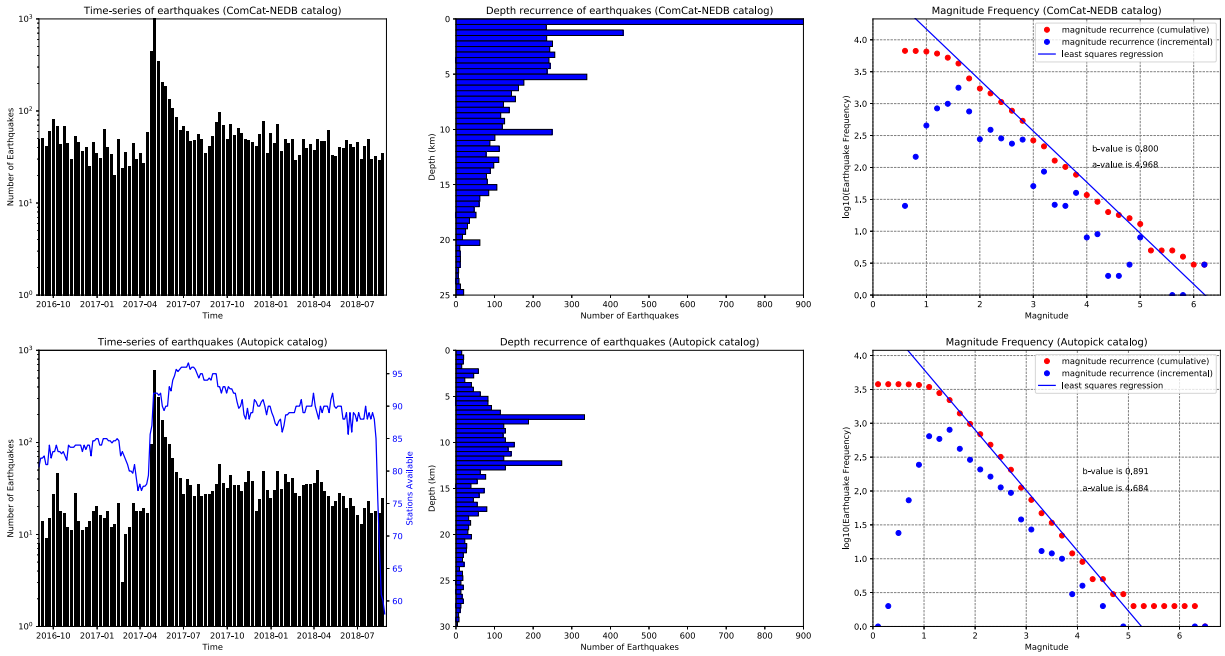

Figure 2.7: Population statistics for the USGS ComCat and Natural Resources Canada catalogs (top row) and the *REST* catalog (bottom row) in the large study region. Left) Histogram of earthquake recurrence. Binned in 7 day increments and overlain by a plot of station availability (*REST* catalog only). Center) Depth histogram with artificially inflated bins at 0, 5, and 12.5 km depth in the ComCat-NEDB catalog, and 2.5, 7.5, 12.5, and 17.5 km depth in the *REST* catalog. Right) Magnitude-frequency plots. Red circles are the cumulative magnitude distribution, blue circles are incremental. The slope of the blue line is the log-linear *b*-value.

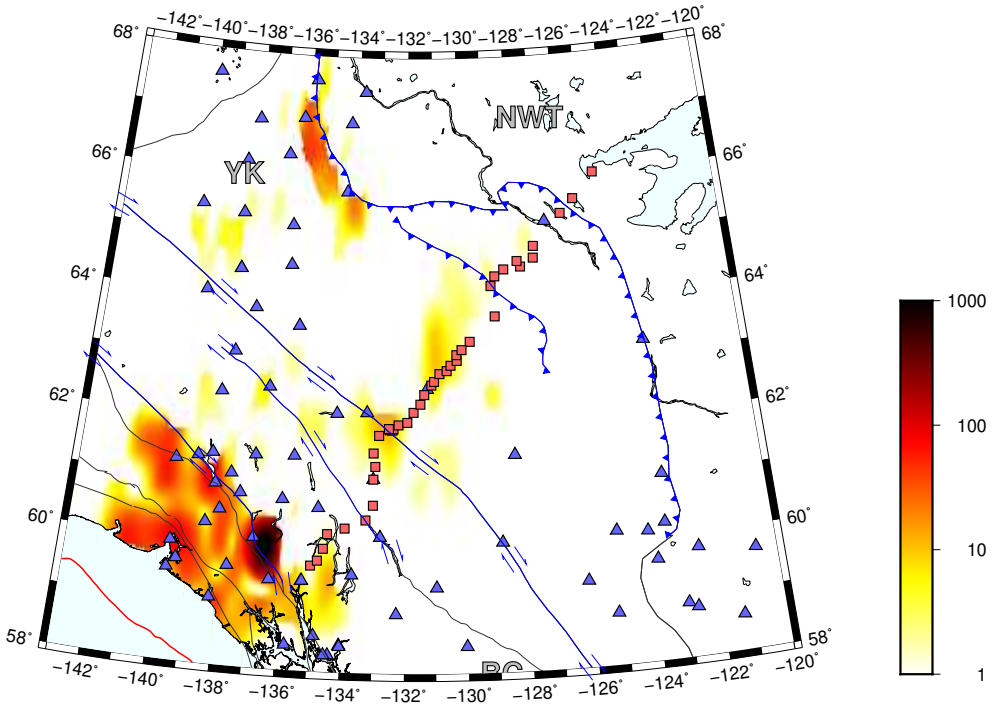

Figure 2.8: Logarithmic scale heatmap representing the number of earthquakes detected by the *REST* software. Events are binned in half-degree (0.5°Latitude x 0.5°Longitude) increments.

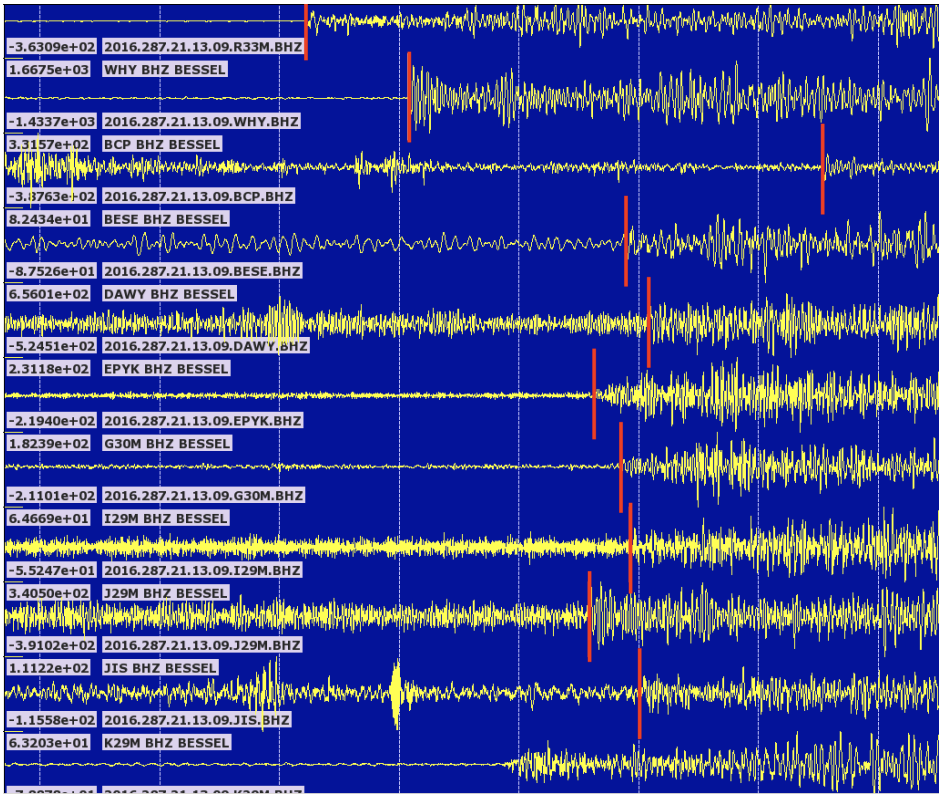

Figure 2.9: Picked phase arrivals (red vertical line) displayed in Gphase (Roecker, unpublished) for a M 4.1 event on 13 October 2016. Note that some arrivals are not picked for certain phases. This is a shortcoming of the automatic detection algorithm, in that it does not perform with 100% accuracy.

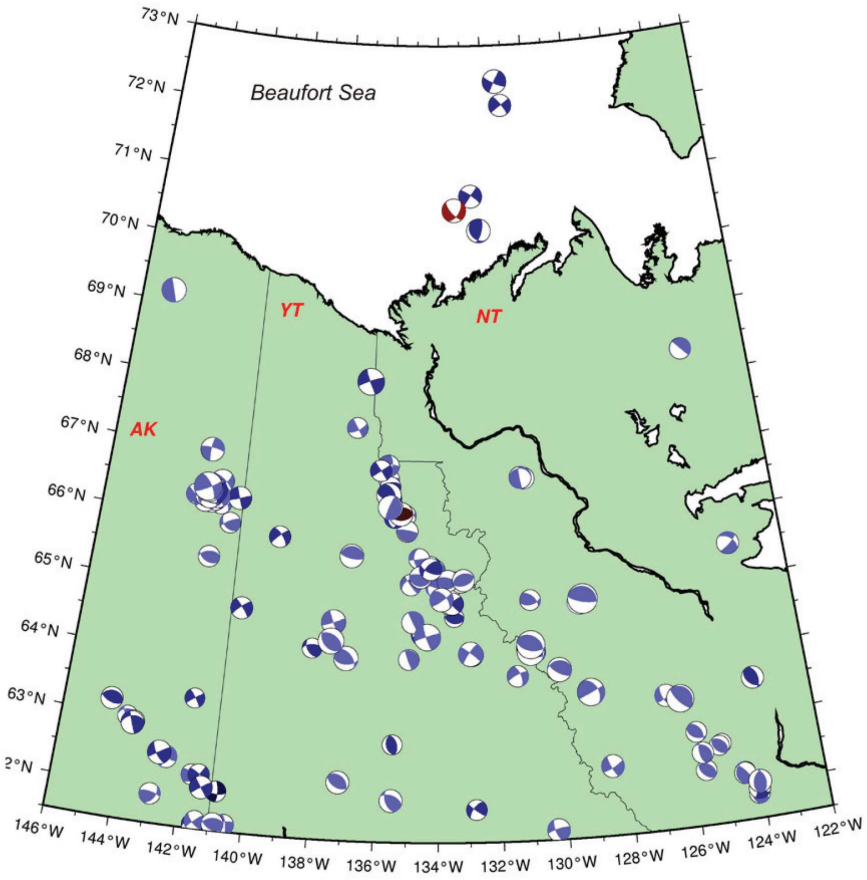

Figure 2.10: Moment tensor solutions for the Mackenzie Mountains (modified from Kao et al. (2012)). A plot of regional CMT solutions in the Mackenzie Mountains and surrounding regions.

Chapter 3

Getting Started with REST

This Chapter will assist users of the *REST* software package with reproducing the results discussed in Chapter 2, introduce techniques to inspect those results in new ways, and present options for modifying the parameters of this study to generate a new catalog. This document will broadly serve as a user manual, with examples and instructions for each stage of the workflow. Further documentation exists within the software (READMEs, Microsoft Word documents, and comments in programs), to which users will be appropriately referred throughout this manual. Topics discussed herein will include the various dependencies necessary to run the software, an outline of the organization of the code repository, instructions for modifying parameters for future experiments, and a discussion about the future applications of this software package.

3.1 Dependencies

Several compilers and programming environments are either necessary or useful to run the *REST* software. The following items should be installed prior to beginning:

- The **GNU Compiler Collection** (*gcc*) and one of its components, *gfortran*, are free, publicly available compilers necessary for compiling various C and FORTRAN routines in the code.
- **CURL**, a utility to transfer data from a server via HTTP or other protocols.
- **Seismic Analysis Code** (SAC), a utility for viewing and manipulating seismic data.
- **csh**, **tcsh**, and **bash** shell availability.
- **Python** (version 3.7 or later) with Obspy, Matplotlib, Numpy, and Pandas packages installed using Anaconda (along with several others, noted at the beginning of the *eq_compare.py* script).
- **Generic Mapping Tools** (GMT) version 5, with the full resolution coastline database.

Each applicable program listed above should be in the user's PATH variable. It is also necessary to include the current directory (".") in your PATH. Additionally, users must obtain a user ID and password from the IRIS DMC in order to access restricted 7C network data. Registration for data access can be applied for at the following link: http://ds.iris.edu/ds/nodes/dmc/forms/restricted-data-registration/.

3.2 Repository Organization

The code repository is located on the Warner College of Natural Resources GEO1 server in the path '/data/seismo/code/REST' and includes two main directories: a raw distribution of the software (latest version as of April 2019), and the modified version(s) used to reproduce the results of this project – titled 'distribution.20190410' and 'REST', respectively.

In the raw distribution directory, the user should primarily make note of the directory 'rest_example' and the scripts *make_package.csh* and *setup_example.csh*. 'rest_example' is an example of the final output of catalog generation for a sample dataset. *make_package.csh* is used to compile all subroutines necessary for *Stage One* (see Chapter 1 Section 1.4.2) and place them in an appropriate location. *setup_example.csh* is used to prepare a test run, to ensure the code is working properly.

The directory of modified code and auxiliary scripts, 'REST', is used to replicate the results of this thesis, as well as perform further analyses or modified studies. There are six directories contained within 'REST'. Their primary purposes are listed below:

- 'One_hr_run' is a simple example of catalog generation, similar to the example provided in the raw distribution. One hour of raw seismic data (containing a known event) are retrieved from the DMC and processed to generate a catalog.

- '3_day_run' is a more involved example, which retrieves two separate 3-day periods of raw data (over the course of which several known events occur), processes these data, and generates a catalog of events.

- 'Full_run' replicates the catalog presented in this thesis in its entirety. The entire 2 years of data are downloaded, processed, and stored in a catalog.
- 'Data_request' contains the scripts for requesting and cleaning raw seismic traces from the IRIS DMC.
- 'Processing_scripts' contains auxiliary scripts useful in data analysis and visualization (*Stage Two*).
- 'Plotting' contains shell scripts for GMT plotting.

3.3 Running the Examples

The user should begin by following the instructions for compiling and installing the necessary programs in the raw distribution (Section 3.2), and then running the example therein. Once completed, the user should attempt to run each of the three modified examples in the 'REST' directory. Lastly, the user should analyze the results of the data utilizing programs in the 'REST/Processing_scripts' and 'REST/Plotting' directories.

3.3.1 Original Distribution

The user is first referred to the 'distribution.20190410/docs' directory for documentation regarding installation of the software and running the example provided. The user should take time now to read the entire manual for an introduction to the capabilities and specifics of the *REST* code. The scripts in this raw distribution should require very little (if any) editing, as the programs are installed in the local directory 'distribution.20190410/bin'. This directory should be subsequently added to the user's PATH variable. Once compiled and installed, the user should switch to the 'distribution.20190410/test' directory (created using the *rest_example.csh* script) and attempt to run the example. The results contained in the 'test' directory should be compared to the 'distribution.20190410/rest_example' directory to ensure they match.

3.3.2 Modified version

Once the example from the raw distribution has run successfully, the user should switch to the 'REST/One_hr_run' directory to process data from the Mackenzie Mountains study region. Unlike in the raw example, data are not provided and are instead retrieved from the IRIS DMC. Note that it is not necessary to download the data more than once – this is discussed in Section 3.5 regarding parameter modifications. The data retrieval and initial processing takes place in the 'REST/Data_request' folder. The script *one_hr_run* should be modified to contain the new IRIS user ID and password, and the appropriate root path. In this script, it is assumed that the top level directory of the code package is located in the user's home directory ("~"). The user is referred to comments in the *one_hr_run* script for information on each processing step. This script will create new directories (similar to the process of initializing the 'distribution.20190410/test' directory) with the correct files created and appropriately formatted.

The 'REST/3_day_run' directory is similar to the previous example, differing only in that the processing time is greatly increased, and loops are introduced to run multiple subsets of 5-day time periods. Recall that the user should include their own IRIS user ID and password, and modify the root path variable in the *three_hour_run* script.

Finally, the 'REST/Full_run' directory contains the script necessary to entirely reproduce the results of this thesis. The user should once again modify the *full_run* script appropriately. Note, this script takes approximately 3 weeks to run.

Traveltime Table Calculations

In accordance with the methodology described in Chapter 1 Section 2.6.4, traveltime tables should be calculated once for the set of all potential stations for which data might exist (i.e., certain temporary stations may have only been deployed for a fraction of the total study period, but must have a traveltime table nonetheless). An initial velocity model is required for this step. The amalgamated Ma and Audet (2017) and Schaeffer and Lebedev (2014) are provided by default. Additional velocity models by Kennett et al. (1995) and D. Schutt (2019, personal communication) are also included for optional use. Traveltime table calculations are computed with the

make_travel_time_tables script located in the 'REST/Data_request' directory. Specific instructions regarding running this script are included in the 'REST/Data_request/README' file, since the special workflow to calculate traveltime tables begins with a unique data request.

3.4 Data Analysis Scripts

Upon completion of any of the previous steps, the user has the option to analyze the results of their data. Broadly, areas of analysis include seismic statistics and geographic plotting routines. Simple steps to get started involve copying the final catalog of earthquake locations (typically *fdloc.magheads.WINDOWS*) to the 'REST/Processing_scripts' directory, modifying the root directory in the *py_filter.bash* script, and then following the instructions in the README file (in the 'REST/Processing_scripts' directory) to perform the desired calculations. This directory contains a combination of Python and bash scripts for various processing routines, described below.

3.4.1 Time, Depth, and Magnitude Recurrence

The Python script *eq_compare.py* performs a majority of the calculations available to the user. Primarily, this script compares the results of the *REST*-generated catalog to records maintained by the USGS. The user should provide a slightly modified USGS catalog (for more inforation regarding the format of this catalog, the user is referred again to the README file in 'REST/Prociessing_scripts') and the *fdloc.magheads.WINDOWS* catalog generated by the *REST* software. The user should first run *py_filter.bash*, and then edit (as necessary) the file names in the *eq_compare.py* script, where noted. The user should then execute the Python script in an initialized environment (see Chapter 3 Section 3.1), which will calculate statistical properties of the new catalog as well as measures of comparison against the USGS catalog. The number of unique events, similar events, and non-located events between the *REST* and USGS catalogs are calculated, as well as temporal and spatial deviations between the matching events. Statistical properties such as the *a*- and *b*-values of the magnitude recurrence plots are also displayed, as well as regressed variables for relationship assessment.

3.4.2 Plotting

After running *eq_compare.py*, the user should execute the bash script *clean_eq_catalog.bash* to prepare the modified catalogs (e.g., the catalog of matching *REST* and USGS-maintained events) for plotting in GMT. This script formats the catalogs and places them in the plotting directory. The user can then switch to the 'REST/Plotting' directory and run the plotting script therein to generate a suite of plots. The functional description and scaling interpretations are described in comments at the top of each plotting script.

3.5 Parameter Modification

Initially, only certain variables in the main scripts within the 'One_hr_run', '3_day_run', and 'Full_run' directories should be modified (see Chapter 3 Section 3.3.2). However, the user has the option to modify several additional parameters in these scripts for improved customization to the study region. In each of the modified example directories a template directory is contained therein, from which all other directories in that run are copied. Files should be edited in the template directory so that the changes propagate from a common source. An example of one likely change involves editing the *make_all_files* script to run only a subset of the data. Changes to the '*.spec' files are the primary way in which parameters are modified. For more information regarding user-specified variable options and modification, the user is referred to the documentation contained in 'distribution.20190410/docs'.

Optimal parameters vary primarily by the geographic region of the study area and the level of seismic activity (e.g., aftershock sequence vs. quiet period). A small subset of data with known events should be used to first hone parameters custom to the study region. Certain specification files include an option to save the otherwise temporary output files that show the selection criterion for detections, events, windows, etc. These options should be turned on during the parameter calibration period, and turned off again before running the full dataset (to save storage space and computation time). The user should decide where they find the optimal trade-off between sensitivity to possible events and computation time. If the parameters are not adequately sensitive to both

impulsive and emergent signals, events will be missed. However, overly sensitive parameters will increase computation time and the storage required for generating a large catalog. In general, the user should note that without detecting an event early in the processing steps it is very unlikely that it will be noticed in later stages. Beginning with high sensitivity (e.g., low *pfact* value, high uncertainty windows in 'rest.spec', etc.) and then moving to more strict criteria is always the suggested workflow.

Additionally, the IRIS DMC data request is a time and memory-intensive operation. Rather than require the user to re-download all data for subsequent runs, a modified script is provided – *rerun*. This script allows for modifications to the original "template" directory, and will copy all changes to the appropriate locations without overwriting or deleting the SAC files therein. In this way, the runtime is shortened by approximately 50%. For simple parameter modifications in only one run directory, the user can still manually run the *make_clean*, *make_all_files*, and *make_catalog* scripts (which also does not delete the downloaded SAC files).

Lastly, the user should note that generating a final catalog with some false events is difficult to avoid. It is advisable to allow some false events to permeate than to unnecessarily eliminate real events with overly strict parameters. The reported confidence values, number of phases used, residual time, and azimuthal coverage can all give hints about the existence of false events. Additionally, spot-checking record sections is useful in ensuring the accuracy of the catalog generation.

3.6 Future Modifications and Capabilities

As inputs to the *REST* software are improved, the 'Full_Run' directory should be appropriately modified and re-run. Improvements to the velocity model or station data availability should be identified as critically important inputs to improve the earthquake catalog. Traveltime table calculation improvements and increased azimuthal coverage can significantly aid in location algorithms employed by the *REST* software. Additionally, minor changes in the custom parameters specified in the user-defined **.spec* files are always encouraged, to better represent the choices of

an actual earthquake analyst. Whenever modifications are made, the *REST* code should be tested over a small subset of data before re-running the entire deployment period.

Additionally, the *REST* software can be used anywhere in the world where a velocity model exists and there are seismometers located within the region of interest. Region-specific customization should be tested (as always) over a small subset of data with known events, before generating a large catalog.

3.7 Computational Limitations

Several shortcomings of the *REST* software were identified over the course of this experiment. In the sections that follow, those issues and their potential solutions will be discussed.

3.7.1 Aftershock Sequences

For highly seismically active periods of time, such as in the immediate aftermath of a large-magnitude earthquakes, during which aftershocks are occurring, the *REST* software can fail to locate many events. If earthquakes are "overlapping" (i.e., signals from one earthquake are still arriving at far away stations when another earthquake occurs) the location algorithm has a difficult time distinguishing between the different events. Because the traces are windowed in the same absolute time window for every seismogram, in these instances the software may identify arrivals within seconds of each other on opposite ends of the array. This effectively breaks the location algorithm.

One possible fix for this issue involves "smart windowing." In this experimental workflow, each trace would be windowed about a *relative* arrival time, rather than a one-size-fits-all approach of an absolute time window for every seismogram. Additionally, for an aftershock sequence there should be a similar location from which all other earthquakes originate. This can be used to identify a starting location for record section plots, from which a ray parameter can be calculated, using the first arrivals at the nearest stations. This ray parameter should be used to guide the smart windowing process such that – within a certain tolerance – those later arrivals are added to

the event-specific location algorithms. Utilizing this experimental workflow should dramatically improve the efficacy of the *REST* software in aftershock sequences.

In this experiment, our results were limited by the inability to capture overlapping earthquakes. Given the very large study area, overlapping events were likely captured (and subsequently discarded) even outside of an aftershock sequence.

3.8 Future Studies

The results of this study should be used to inform models of local tomography in the study region, such as through use of the complimentary *tomoFD* software (Roecker, unpublished). The workflow required to run *tomoFD* is similar to that of *REST*, with the primary difference being that the updated velocity model is saved across the duration of the processing workflow (Presently, the updated velocity model is discarded after each event location is determined. See Chapter 2 Section 2.6.4 for more information.). Station-event pick times and an initial velocity model can be used to calculate heterogeneities in the velocity structure of the lithosphere. A high-resolution earthquake catalog with hundreds or thousands of events, such as this one, should inform a well-resolved tomographic model.

Additionally, earthquake location, magnitude, and recurrence data can inform seismic hazards models in the study region. Further, the active faults identified in this study can be re-located with greater accuracy through methods such as double difference relocation.

In the remote Yukon and Northwest Territories, public information campaigns would prove an additionally useful endeavor. As studies have shown (e.g., Hyndman et al., 2005a), these populations are largely uninformed about the risks posed by earthquakes. Distributing information regarding earthquake readiness and real-time safety actions is thus advisable.

Bibliography

Adams, J. and Atkinson, G. (2003). Development of seismic hazard maps for the proposed 2005 edition of the National Building Code of Canada. *Canadian Journal of Civil Engineering*, 30(2):255–271.

Aki, K. (1965). Maximum likelihood estimate of b in the formula log n= a-bm and its confidence limits. *Bull. Earthq. Res. Inst., Tokyo Univ.*, 43:237–239.

Aki, K. and Richards, P. (1980). Quantitative Seismology: Theory and Methods, 1980, vol. 1 & 2.

Allam, A., Ben-Zion, Y., and Peng, Z. (2014). Seismic imaging of a bimaterial interface along the Hayward fault, CA, with fault zone head waves and direct P arrivals. *Pure and Applied Geophysics*, 171(11):2993–3011.

Audet, P., Currie, C. A., Schaeffer, A. J., and Hill, A. M. (2019). Seismic evidence for lithospheric thinning and heat in the Northern Canadian Cordillera. *Geophysical Research Letters*, 46(8):4249–4257.

Baker, M. G., Heath, D. C., Schutt, D. L., Aster, R. C., Cubley, J. F., and Freymueller, J. T. (2020). The Mackenzie Mountains EarthScope Project: Studying active deformation in the northern North American Cordillera from margin to craton. *Seismological Research Letters*, 91(1):521–532.

Brocher, T. M. (2005). Empirical relations between elastic wavespeeds and density in the Earth's crust. *Bulletin of the Seismological Society of America*, 95(6):2081–2092.

Bruns, T. R. (1983). Model for the origin of the Yakutat block, an accreting terrane in the northern Gulf of Alaska. *Geology*, 11(12):718–721.

Cao, A. and Gao, S. S. (2002). Temporal variation of seismic b-values beneath northeastern Japan island arc. *Geophysical Research Letters*, 29(9):48–1.

Coney, P. J., Jones, D. L., and Monger, J. W. (1980). Cordilleran suspect terranes. *Nature*, 288(5789):329.

Cornell, C. A. (1968). Engineering seismic risk analysis. *Bulletin of the Seismological Society of America*, 58(5):1583–1606.

Enkelmann, E., Finzel, E., and Arkle, J. (2019). Deformation at the eastern margin of the northern Canadian Cordillera: Potentially related to opening of the North Atlantic. *Terra Nova*.

Finn, W. (2000). State-of-the-art of geotechnical earthquake engineering practice. *Soil Dynamics and Earthquake Engineering*, 20(1-4):1–15.

Finzel, E. S., Flesch, L. M., Ridgway, K. D., Holt, W. E., and Ghosh, A. (2015). Surface motions and intraplate continental deformation in Alaska driven by mantle flow. *Geophysical Research Letters*, 42(11):4350–4358.

Fletcher, H. J. and Freymueller, J. T. (2003). New constraints on the motion of the Fairweather fault, Alaska, from GPS observations. *Geophysical Research Letters*, 30(3).

Flück, P., Hyndman, R., and Lowe, C. (2003). Effective elastic thickness Te of the lithosphere in western Canada. *Journal of Geophysical Research: Solid Earth*, 108(B9).

Freymueller, J, H. R. and Woodward, B. (2013). Report on Workshop USArray-Alaska extension into northwestern Canada: Earthscope. Technical report, Pacific Geoscience Centre, Geological Survey of Canada.

Frohlich, C. and Davis, S. D. (1993). Teleseismic b values; or, much ado about 1.0. *Journal of Geophysical Research: Solid Earth*, 98(B1):631–644.

Gabrielse, H. (1991). Geology of the Cordilleran orogen in Canada. *Geological Society of America, Geology of North America*, page 844.

Ghosh, A., Holt, W. E., and Bahadori, A. (2019). Role of large-scale tectonic forces in intraplate earthquakes of central and eastern North America. *Geochemistry, Geophysics, Geosystems*.

Gomberg, J. S., Shedlock, K. M., and Roecker, S. W. (1990). The effect of S-wave arrival times on the accuracy of hypocenter estimation. *Bulletin of the Seismological Society of America*, 80(6A):1605–1628.

Gutenberg, B. and Richter, C. F. (1944). Frequency of earthquakes in California. *Bulletin of the Seismological Society of America*, 34(4):185–188.

Halchuk, S., Adams, J., and Allen, T. (2015). Fifth generation seismic hazard model for canada: Grid values of mean hazard to be used with the 2015 National Building Code of Canada. *Geological Survey of Canada, Open File*, 7893:26.

Hanks, T. C. and Kanamori, H. (1979). A moment magnitude scale. *Journal of Geophysical Research: Solid Earth*, 84(B5):2348–2350.

Hole, J. and Zelt, B. (1995). 3-d finite-difference reflection traveltimes. *Geophysical Journal International*, 121(2):427–434.

Hyndman, R. (2017). Lower-crustal flow and detachment in the North American Cordillera: a consequence of Cordillera-wide high temperatures. *Geophysical Journal International*, 209(3):1779–1799.

Hyndman, R., Cassidy, J., Adams, J., Rogers, G., and Mazzotti, S. (2005a). Earthquakes and seismic hazard in the Yukon-Beaufort-Mackenzie. *CSEG Recorder*, pages 32–66.

Hyndman, R., Currie, C., Mazzotti, S., and Frederiksen, A. (2009). Temperature control of continental lithosphere elastic thickness, Te vs Vs. *Earth and Planetary Science Letters*, 277(3-4):539–548.

Hyndman, R. and Lewis, T. (1999). Geophysical consequences of the Cordillera–Craton thermal transition in southwestern Canada. *Tectonophysics*, 306(3-4):397–422.

Hyndman, R. D., Flück, P., Mazzotti, S., Lewis, T. J., Ristau, J., and Leonard, L. (2005b). Current tectonics of the northern Canadian Cordillera. *Canadian Journal of Earth Sciences*, 42(6):1117–1136.

James, T., Mazzotti, S., Mazzotti, S., and Lambert, A. (2001). Constraints on the mid-continent deformation gravity gradient determined from co-located GPS and absolute gravity observations. In *AGU Fall Meeting Abstracts*.

Johnston, S. T. (2001). The great Alaskan terrane wreck: reconciliation of paleomagnetic and geological data in the northern Cordillera. *Earth and Planetary Science Letters*, 193(3-4):259–272.

Kao, H., Shan, S.-J., Bent, A., Woodgold, C., Rogers, G., Cassidy, J. F., and Ristau, J. (2012). Regional centroid-moment-tensor analysis for earthquakes in Canada and adjacent regions: An update. *Seismological Research Letters*, 83(3):505–515.

Kennett, B. L., Engdahl, E., and Buland, R. (1995). Constraints on seismic velocities in the Earth from traveltimes. *Geophysical Journal International*, 122(1):108–124.

Kushnir, A., Lapshin, V., Pinsky, V., and Fyen, J. (1990). Statistically optimal event detection using small array data. *Bulletin of the Seismological Society of America*, 80(6B):1934–1950.

Leonard, L. J., Mazzotti, S., and Hyndman, R. D. (2008). Deformation rates estimated from earthquakes in the northern Cordillera of Canada and eastern Alaska. *Journal of Geophysical Research: Solid Earth*, 113(B8).

Lewis, T., Hyndman, R., and Flück, P. (2003). Heat flow, heat generation, and crustal temperatures in the northern Canadian Cordillera: thermal control of tectonics. *Journal of Geophysical Research: Solid Earth*, 108(B6).

Ma, S. and Audet, P. (2017). Seismic velocity model of the crust in the northern Canadian Cordillera from Rayleigh wave dispersion data. *Canadian Journal of Earth Sciences*, 54(2):163–172.

Marechal, A., Mazzotti, S., Elliott, J. L., Freymueller, J. T., and Schmidt, M. (2015). Indentor-corner tectonics in the Yakutat-St. Elias collision constrained by GPS. *Journal of Geophysical Research: Solid Earth*, 120(5):3897–3908.

Mazzotti, S. and Hyndman, R. D. (2002). Yakutat collision and strain transfer across the northern Canadian Cordillera. *Geology*, 30(6):495–498.

Mogi, K. (1962). Magnitude-frequency relation for elastic shocks accompanying fractures of various materials and some related problems in earthquakes. *Bull. Earthq. Res. Inst.*, 40:831–853.

Mori, J. and Abercrombie, R. E. (1997). Depth dependence of earthquake frequency-magnitude distributions in California: implications for rupture initiation. *Journal of Geophysical Research: Solid Earth*, 102(B7):15081–15090.

Natural Resources Canada (2019). Earthquakes Canada, GSC, Earthquake Search (On-line Bulletin). http://earthquakescanada.nrcan.gc.ca/stndon/NEDB-BNDS/bulletin-en.php.

Nelson, J. and Colpron, M. (2007). Tectonics and metallogeny of the British Columbia, Yukon and Alaskan Cordillera, 1.8 Ga to the present. *Mineral Deposits of Canada: A Synthesis of Major Deposit-Types, District Metallogeny, the Evolution of Geological Provinces, and Exploration Methods. Edited by WD Goodfellow. Geological Association of Canada, Mineral Deposits Division, Special Publication*, 5:755–791.

Nelson, J., Colpron, M., Israel, S., Bissig, T., Rusk, B., and Thompson, J. (2013a). The Cordillera of British Columbia, Yukon, and Alaska: Tectonics and metallogeny. *Tectonics, Metallogeny, and Discovery: The North American Cordillera and Similar Accretionary Settings: Society of Economic Geologists Special Publication*, 17:53–109.

Nelson, J. L., Colpron, M., Israel, S., Bissig, T., Rusk, B. G., and Thompson, J. F. H. (2013b). The Cordillera of British Columbia, Yukon, and Alaska: Tectonics and metallogeny. In Colpron, M., Bissig, T., Rusk, B. G., and Thompson, J. F. H., editors, *Tectonics, Metallogeny, and Discovery:*

The North American Cordillera and Similar Accretionary Settings, pages 53–109. Society of Economic Geologists.

Nikolov, S. (2012). *Trend or no trend: a novel nonparametric method for classifying time series*. PhD thesis, Massachusetts Institute of Technology.

Nuttli, O. W. (1973). Seismic wave attenuation and magnitude relations for eastern North America. *Journal of Geophysical Research*, 78(5):876–885.

Oldow, J. S., Bally, A. W., and AveÌĄ Lallemant, H. G. (1990). Transpression, orogenic float, and lithospheric balance. *Geology*, 18(10):991–994.

Pomeroy, P. W., Best, W. J., and McEvilly, T. V. (1982). Test ban treaty verification with regional data - a review. *Bulletin of the Seismological Society of America*, 72(6B):S89–S129.

Powell, J. (2017). *Burial and exhumation history of the Mackenzie Mountains and Plain, NWT, through integration of low-temperature thermochronometers*. PhD thesis, Université d'Ottawa/University of Ottawa.

Rawles, C. and Thurber, C. (2015). A non-parametric method for automatic determination of P-wave and S-wave arrival times: application to local micro earthquakes. *Geophysical Journal International*, 202(2):1164–1179.

Richter, D. and Matson Jr, N. (1971). Quaternary faulting in the eastern Alaska Range. *Geological Society of America Bulletin*, 82(6):1529–1540.

Ristau, J. P. (2004). *Seismotectonics of western Canada from regional moment tensor analysis*. PhD thesis, University of Victoria.

Rocha, M. P., de Azevedo, P. A., Marotta, G. S., Schimmel, M., and Fuck, R. (2016). Causes of intraplate seismicity in central Brazil from travel time seismic tomography. *Tectonophysics*, 680:1–7.

Roddick, J. (1967). Tintina trench. *The Journal of Geology*, 75(1):23–33.

Roecker, S., Thurber, C., Roberts, K., and Powell, L. (2006). Refining the image of the San Andreas Fault near Parkfield, California using a finite difference travel time computation technique. *Tectonophysics*, 426(1-2):189–205.

Russell, J. K., Dipple, G., and Kopylova, M. (2001). Heat production and heat flow in the mantle lithosphere, Slave craton, Canada. *Physics of the Earth and Planetary Interiors*, 123(1):27–44.

Rutter, E. (1986). On the nomenclature of mode of failure transitions in rocks. *Tectonophysics*, 122(3-4):381–387.

Rydelek, P. A. and Sacks, I. S. (1989). Testing the completeness of earthquake catalogues and the hypothesis of self-similarity. *Nature*, 337(6204):251.

Schaeffer, A. and Lebedev, S. (2014). Imaging the North American continent using waveform inversion of global and USArray data. *Earth and Planetary Science Letters*, 402:26–41.

Scholz, C. H. (1998). Earthquakes and friction laws. *Nature*, 391(6662):37.

Scholz, C. H. (2015). On the stress dependence of the earthquake b value. *Geophysical Research Letters*, 42(5):1399–1402.

Shoja-Taheri, J. and Niazi, M. (1981). Seismicity of the Iranian plateau and bordering regions. *Bulletin of the Seismological Society of America*, 71(2):477–489.

Sibson, R. H. (1990). Rupture nucleation on unfavorably oriented faults. *Bulletin of the Seismological Society of America*, 80(6A):1580–1604.

Smith, R. B. and Bruhn, R. L. (1984). Intraplate extensional tectonics of the eastern Basin-Range: Inferences on structural style from seismic reflection data, regional tectonics, and thermal-mechanical models of brittle-ductile deformation. *Journal of Geophysical Research: Solid Earth*, 89(B7):5733–5762.

Spada, M., Tormann, T., Wiemer, S., and Enescu, B. (2013). Generic dependence of the frequency-size distribution of earthquakes on depth and its relation to the strength profile of the crust. *Geophysical Research Letters*, 40(4):709–714.

Sykes, L. R. (1978). Intraplate seismicity, reactivation of preexisting zones of weakness, alkaline magmatism, and other tectonism postdating continental fragmentation. *Reviews of Geophysics*, 16(4):621–688.

Talwani, P. (1989). Characteristics features of intraplate earthquakes and the models proposed to explain them. *NATO ASI series. Series C, Mathematical and physical sciences*, 266:563–579.

Tape, C., Heath, D. C., Baker, M. G., Dalton, S., Aderhold, K., and West, M. E. (2019). Bear encounters with seismic stations in Alaska and northwestern Canada. *Seismological Research Letters*, 90(5):1950–1970.

Tarantola, A. and Valette, B. (1982). Generalized nonlinear inverse problems solved using the least squares criterion. *Reviews of Geophysics*, 20(2):219–232.

Vidale, J. E. (1990). Finite-difference calculation of traveltimes in three dimensions. *Geophysics*, 55(5):521–526.

Wald, D., Jaiswal, K., Marano, K., Bausch, D., and Hearne, M. (2011). PAGER Rapid assessment of an earthquake's impact. *U.S. Geological Survey Fact Sheet 2010-3036*, pages 1–4.

Wiemer, S. and Schorlemmer, D. (2007). Alm: An asperity-based likelihood model for California. *Seismological Research Letters*, 78(1):134–140.

Worthington, L. L., Van Avendonk, H. J., Gulick, S. P., Christeson, G. L., and Pavlis, T. L. (2012). Crustal structure of the Yakutat terrane and the evolution of subduction and collision in southern Alaska. *Journal of Geophysical Research: Solid Earth*, 117(B1).

Appendix A

Station Information

Table A.1: Station information for each seismograph utilized in processing for the *REST* catalog.

Network	Station	Latitude	Longitude	Elevation (m)
7C	MM01	59.7153	-135.0510	885
7C	MM02	59.8029	-134.8387	753
7C	MM03	59.9992	-134.6654	698
7C	MM04	60.2400	-134.5509	840
7C	MM05	60.3412	-133.9864	831
7C	MM06	60.4834	-133.3060	715
7C	MM07	60.7272	-133.0708	852
7C	MM08	61.1496	-133.0788	850
7C	MM09	61.3568	-133.0210	939
7C	MM10	61.5744	-133.0906	1138
7C	MM11	61.8624	-132.9147	967
7C	MM12	61.9525	-132.4607	880
7C	MM13	61.9564	-132.5498	863
7C	MM14	61.9733	-132.4257	731
7C	MM15	61.9764	-132.5815	803
7C	MM16	62.0378	-132.2521	772
7C	MM17	62.0789	-131.9483	1023
7C	MM18	62.2424	-131.7340	827
7C	MM19	62.3754	-131.4946	862
7C	MM20	62.5322	-131.3588	915
7C	MM21	62.6859	-131.1073	945

Network	Station	Latitude	Longitude	Elevation (m)
7C	MM22	62.7440	-131.0108	928
7C	MM23	62.8713	-130.8161	984
7C	MM24	62.9184	-130.5585	979
7C	MM25	63.0049	-130.4190	1080
7C	MM26	63.0810	-130.1928	1137
7C	MM27	63.1749	-130.2005	1188
7C	MM28	63.3863	-129.7090	1588
7C	MM29	63.7846	-128.7663	1168
7C	MM30	64.2803	-128.8747	1220
7C	MM31	64.4351	-128.7162	1117
7C	MM32	64.5422	-128.3708	1207
7C	MM33	64.5754	-127.7338	1438
7C	MM34	64.6682	-127.8535	1003
7C	MM35	64.7072	-127.2314	786
7C	MM36	64.8969	-127.2010	562
7C	MM38	65.4005	-126.0765	119
7C	MM39	65.6226	-125.5396	281
7C	MM40	66.0246	-124.6709	159
7C	MM41	63.2552	-130.0124	1428
AK	BCP	59.9534	-139.6369	421
AK	BESE	58.5792	-134.8559	867
AK	DCPH	59.0906	-138.2154	674
AK	JIS	58.2758	-134.3848	10
AK	PNL	59.6670	-139.4014	586
AT	SKAG	59.4601	-135.3289	134

Network	Station	Latitude	Longitude	Elevation (m)
AT	YKU2	59.5121	-139.6711	10
CN	DAWY	64.0647	-139.3937	771
CN	DLBC	58.4372	-130.0272	978
CN	FNBB	58.8903	-123.0099	618
CN	WHY	60.6597	-134.8825	1273
PN	SKGA	59.4650	-135.3098	0
PO	NOWN	65.2943	-126.7145	186
TA	EPYK	66.3701	-136.7191	717
TA	G29M	66.9116	-138.0223	572
TA	G30M	66.9808	-136.2216	739
TA	G31M	66.9227	-134.2708	61
TA	H29M	66.2191	-138.3689	480
TA	H31M	65.8052	-134.3426	642
TA	I28M	65.4483	-139.9355	1188
TA	I29M	65.3609	-138.3063	602
TA	I30M	65.2225	-136.3767	1399
TA	J29M	64.4530	-138.2158	982
TA	J29N	64.4525	-138.2164	982
TA	J30M	64.5753	-136.3304	1419
TA	K29M	63.8433	-137.5201	1367
TA	L29M	63.1090	-138.1290	918
TA	M29M	62.4435	-138.4624	1297
TA	M30M	62.5763	-136.7935	782
TA	M31M	62.2024	-134.3906	639
TA	N30M	61.4593	-137.0885	941

Network	Station	Latitude	Longitude	Elevation (m)
TA	N31M	61.4862	-135.7796	716
TA	N32M	61.1512	-133.0818	816
TA	O29M	60.3024	-138.5755	1423
TA	O30N	60.7704	-136.0906	821
TA	P29M	59.6304	-137.7381	679
TA	P30M	60.1218	-136.9598	883
TA	P32M	59.5898	-133.7140	793
TA	P33M	60.2114	-132.8174	1066
TA	Q32M	58.9601	-132.2691	1951
TA	R31K	58.4133	-135.7398	15
TA	R32K	58.2747	-134.5181	386
TA	R33M	59.3946	-130.9673	1437
CN	BRWY	61.3704	-139.0338	2
CN	FNSB	58.8061	-122.7328	40
CN	HYT	60.8267	-137.5072	373
CN	NAHA	61.0311	-123.3902	51
CN	NBC1	59.6559	-123.8237	21
CN	NBC2	59.7735	-122.4878	86
CN	NBC3	59.6372	-120.6687	52
CN	NBC6	58.5839	-121.3339	45
CN	PLBC	59.4550	-136.3659	85
CN	YUK4	61.4348	-138.5463	9
CN	YUK5	61.1315	-137.8593	619
CN	YUK6	60.9432	-138.3626	236
CN	YUK7	60.5307	-138.1399	992

Network	Station	Latitude	Longitude	Elevation (m)
CN	YUK8	61.2844	-139.7646	456
NY	FARO	62.2295	-133.3481	725
NY	FLDN	60.2390	-123.4754	213
NY	MAYO	63.5958	-135.8921	519
NY	MMPY	62.6189	-131.2625	886
NY	TGTN	61.5267	-128.2727	863
NY	WGLY	63.2281	-123.4584	138
NY	WTLY	60.1133	-128.7961	693
TA	F28M	67.6136	-139.8717	64
TA	F30M	67.6106	-135.7863	14
TA	F31M	67.4410	-133.7420	6
YO	BEAV	60.1798	-125.0684	87
YO	KOTA	60.1301	-124.0527	86
YO	LIRD	59.4098	-126.0986	39
YO	TOAD	58.8499	-125.2333	90
ZQ	GAGA	58.4400	-134.0476	58
ZQ	GUGU	58.4201	-134.0387	39

Appendix B

Supplemental Figures

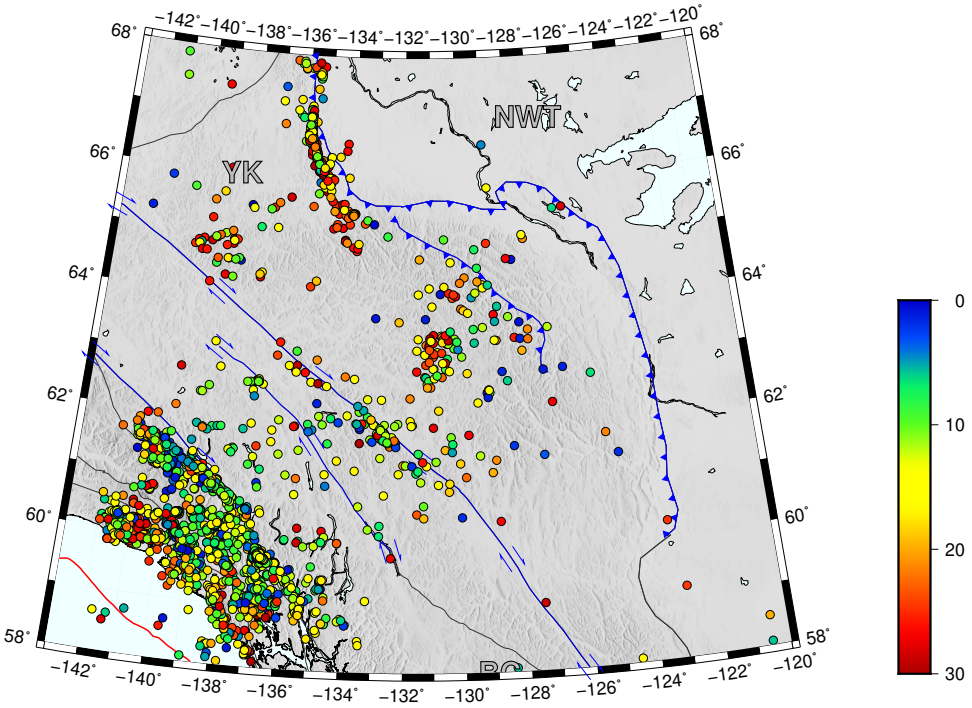

Figure B.1: Hypocenter depths (in km) reported from the *REST* catalog.

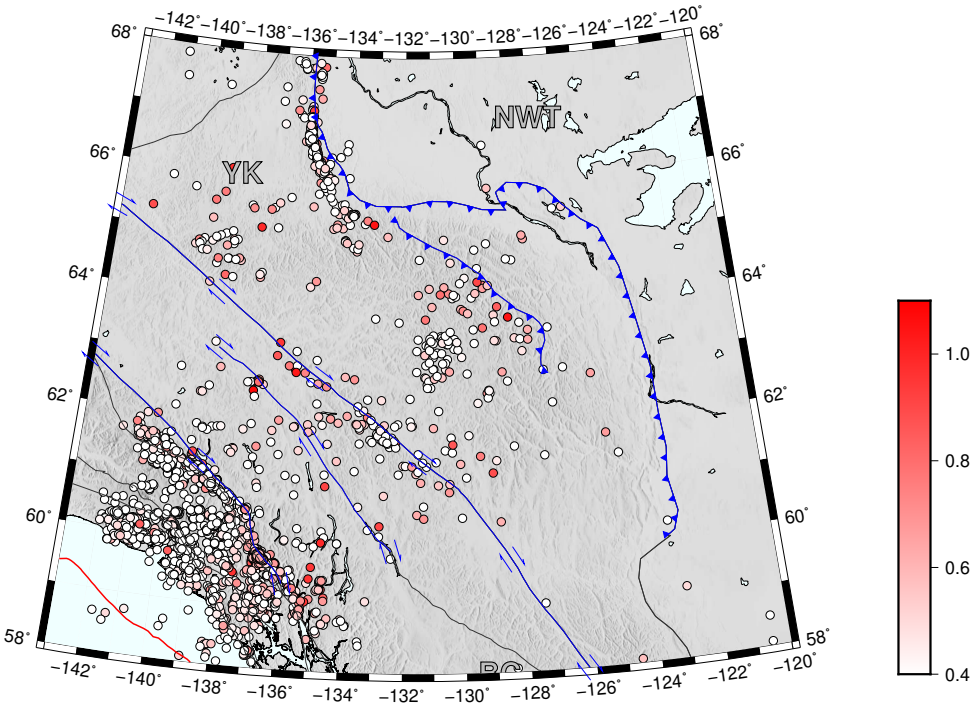

Figure B.2: RMS residuals (in seconds) for each event reported from the *REST* catalog.

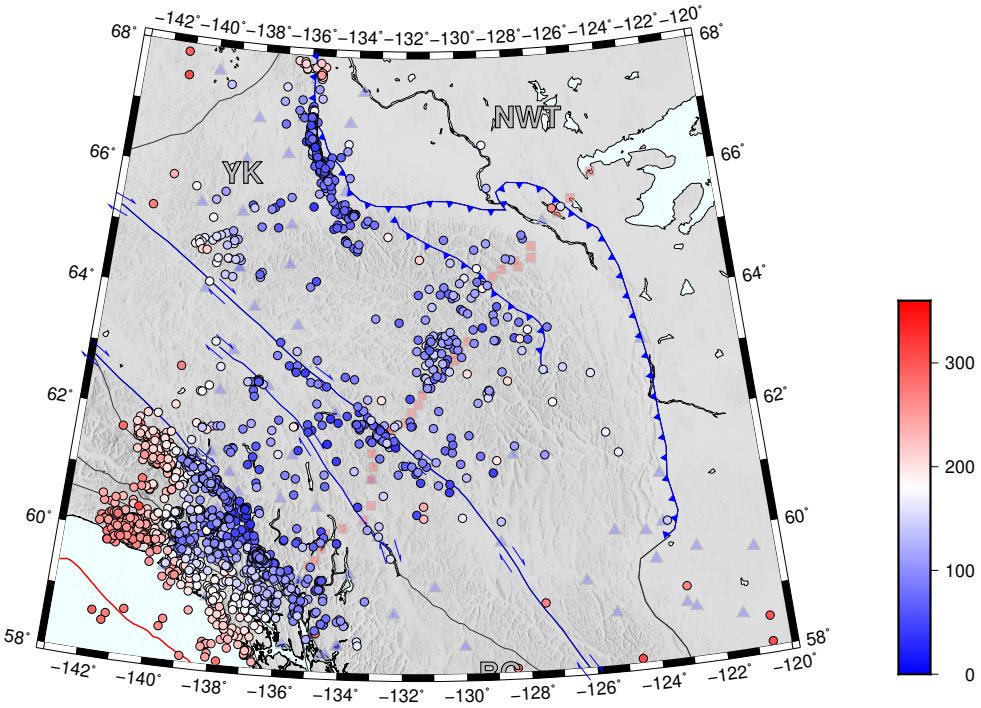

Figure B.3: Azimuthal gap (in degrees) reported from the *REST* catalog.

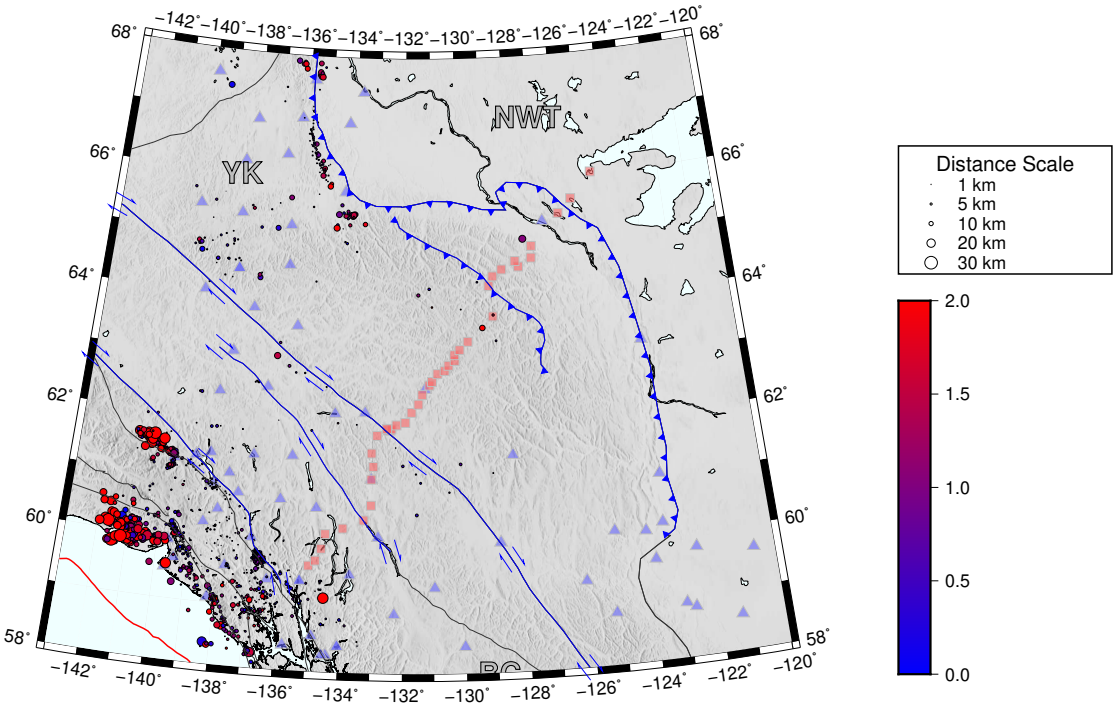

Figure B.4: Matching events scaled by spatial difference (circle radius) in km, and temporal difference (color) in seconds.